

Interactions of Ar^{9+} and metastable Ar^{8+} with a $\text{Si}(100)$ surface at velocities near the image acceleration limit

J. Ducreé*, J. Mrogenda, E. Reckels, M. Rütter, A. Heinen, Ch. Vitt, M. Venier,
J. Leuker, and H.J. Andrä

*Institut für Kernphysik, Westfälische Wilhelms-Universität Münster, Wilhelm-Klemm-Str. 9,
D-48149 Münster, Germany*

R. Díez Muiño

*Laboratoire de Physico-Chimie Théorique, C.N.R.S. et Université de Bordeaux I, 351 Cours de
Libération, 33405 Talence Cedex, France*

(May 4, 2019)

Abstract

Auger *LMM* spectra and preliminary model simulations of Ar^{9+} and metastable Ar^{8+} ions interacting with a clean monocrystalline *n*-doped $\text{Si}(100)$ surface are presented. By varying the experimental parameters, several spectroscopic features have been observed providing valuable information for the development of an adequate interaction model. On our apparatus the ion beam energy can be lowered to almost mere image charge attraction. High data acquisition rates could still be maintained yielding an unprecedented statistical quality of the Auger spectra.

32.80.Dz, 34.50.Dy, 34.70.+e, 36.20.Kd, 79.20.Rf

Typeset using REVTeX

*author to whom correspondence should be addressed. Electronic address: ducree@uni-muenster.de

I. INTRODUCTION

The interactions of highly charged ions (HCI) with surfaces have attracted the strong interest of several research groups in the past, getting a strong boost in the last decade due to the increasing availability of high performance HCI ion sources and improvement of other experimental equipment.

In recent years, various technological applications of HCI surface collisions have been conceived, in particular for the wide field of microscopic and nanoscopic surface modification. In order to foster these efforts, a better understanding of the different stages of the scattering process has to be attained. Experimentalists hope to take advantage of the quick charge exchange processes and the release of the large amount of potential energy stored in the HCI. Unfortunately little consent has been accomplished among researchers on the time scales and the location of these processes although a comprehensive series of spectra and interpretations has been published on this crucial issue so far.

According to the classical overbarrier model [1,2], the neutralization of the HCI sets in at a critical distance of typically $R_c \simeq 15 \text{ \AA}$ in front of the first bulk layer. R_c depends on the target work function W and the initial charge q of the HCI. In the region below R_c , target band electrons are successively captured into resonant ionic Rydberg states with $n \simeq q\sqrt{R_\infty/W}$. As soon as more than two electrons have been transferred, the highly excited hollow atom starts to relax via autoionization processes yielding low-energy electrons. X-ray emission is strongly suppressed for light nuclei. Several studies [3,4] have been carried out showing that the overwhelming fraction of the reflected particles is neutral and suggesting that the projectile charge q is already compensated on the incoming path. Nevertheless, it is commonly accepted by now [5] that the intra-atomic transition rates involved in the cascade are by far too slow to perform a complete relaxation of the neutralized HCI in front of the surface.

Autoionization spectra originating from highly charged ions containing initial inner-shell vacancies are characterized by a strong and intense low-energy region and a uniquely shaped

high-energy branch which can unambiguously be ascribed to intra-atomic transitions involving the inner-shell vacancy. Despite of the low transition rates, certain peak structures can even be associated with Auger emission from fully populated shells neighboring the initial core configuration.

In order to clarify the evolution from Rydberg populations to fully occupied lower shells and motivated by new experimental findings [6–8] about large fractions of subsurface emission within the autoionization spectra, additional interaction mechanisms have been postulated and worked into simulations [9–11]. Also a comparison between Auger spectra for the same HCI projectile impinging on different target species [12] and a new theoretical approach [13] shed new light on the interaction scenario. It seems that the energetic positions of target and projectile electronic states play an important role in all direct inner-shell filling mechanisms below the surface. After the HCI has penetrated into the bulk, band electrons can shield the HCI core charge and directly feed the lower lying hollow atom states while generating a plasmon or an electron hole pair [14,15] (so called *MCV* processes). For projectiles with high kinetic energies, electrons can be directly transferred from bulk atom levels into inner projectile levels yielding a velocity dependent filling rate [9].

In an attempt to extract information on particular transition types from the spectra, experimentalists have analyzed *L*-Auger spectra of Ar^{9+} ions impinging on tungsten [16–19], copper [20] and gold [6]. These early efforts have been obstructed by the large number of initial *M*-shell configurations that had to be considered in the interpretation of the *LMM* spectra with a few distinctive structures only. In recent years, research activities focused on *K*-Auger spectra of hydrogenlike second row ions C^{5+} , N^{6+} , O^{7+} , F^{8+} , Ne^{9+} [8,21–23] and Ar^{17+} [3] instead. Some clearly pronounced peak regions can be identified in most of these spectra and assigned to a comparatively small set of initial *L*-shell configurations. A strong systematic dependence of the relative peak intensities of these *KLL* spectra on the experimental conditions has provided valuable information about the contributing ionic shell configurations.

In this paper, we present several series of *L*-Auger spectra emitted during the interaction

of Ar^{9+} and metastable “heliumlike” Ar^{8+} ions impinging with beam energies between 8eV and 4.6 keV and different experimental geometries on an n-doped Si(100) crystal. For the first time, we discovered significant modifications of the shape of the autoionization spectra for different projectile energies well below 1 keV and for different observation and interaction geometries. They include two geometries that largely suppress the detection of all subsurface electron emission. The so obtained spectra exhibit a unique peak profile that largely deviates from spectra taken under all other experimental geometries.

These effects are very surprising because in the energy regime below 1 keV all collisional M -shell sidefeeding can generally be ruled out and MCV rates can be treated in a static approximation. In order to understand the behavior of the spectra at different incident energies we developed an interaction model taking into account the special role of the $3d$ subshell, which mediates an efficient M -shell filling via valence band electrons within the bulk. Incorporating this model into a Monte Carlo simulation, the observed alterations in the subpeak intensities and positions can qualitatively be reproduced. This model is experimentally supported by a series of L -Auger spectra emitted by metastable Ar^{8+} projectiles. Under the same experimental conditions, the Ar^{8+} LMM Auger peak structures turn out to be amazingly similar to the Ar^{9+} LMM structures.

Section II will introduce to the experimental setup implemented for our measurements. In Section III, we display several sets of autoionization spectra as obtained under specified experimental conditions. Section IV will describe how the LMM subpeaks in our Ar^{9+} spectra can be assigned to particular groups of intra-atomic transitions. The next Section V outlines the basic ingredients of the subsurface interaction model which we employ for the simulation of the Auger spectra. In Section VI, we extract information about the evolution of the projectile neutralization and Auger emission from the combined analysis of experimental observations and the simulation results. Further experimental proof for the portrayed interaction mechanism will be given with the discussion of the L -Auger spectra of metastable Ar^{8+} projectiles in VII. Finally, in VIII, we summarize the basic findings of this paper and give a short outlook on future research.

II. EXPERIMENTAL SETUP

Highly charged ions are extracted by a fixed voltage of -20kV from an ECR ion source, developed in our laboratory. The metallic vacuum chamber of the source can be floated on selectable potentials U_Q with respect to earth potential. These ions are q/m separated by a double focusing sector magnet system including an aberration correction lens. Two electrostatic Einzel lenses convey the beam through the intermediate stages of a differentially pumped vacuum system which is needed to maintain the pressure gradient between the ECR source ($p \simeq 1 \times 10^{-6}\text{mbar}$) and the UHV target chamber ($p \simeq 5 \times 10^{-12}\text{mbar}$). Before hitting the grounded Si wafer, the ions pass through two deceleration lenses which are optimized for a maximum of ions deposited on the target surface of approximately 1cm^2 .

The kinetic ion energy distribution is recorded by an ion spectrometer which is mounted on the beam axis close behind the movable target. For Ar^{9+} and Ar^{8+} beams, the full width at half maximum never exceeded 2eV per charge. The center of the peak is a measure for the kinetic projectile energy after deceleration $E_{\text{kin}} = q(U_Q + U_P)$ where U_P is the plasma potential which builds up between the plasma and the walls of the ECR source. An averaged value of $U_P = 12\text{V}$ has been observed with variations over months of less than $\pm 2\text{V}$. The Si(100) surface has been prepared by successive cycles of Ar^{1+} sputtering at grazing incidence and annealing until all impurities have disappeared from AES spectra and good LEED patterns have shown up.

The geometry within the target chamber is displayed in Fig. 1(a). The beam axis intersects the target surface at an angle Θ . Electrons are detected by an electrostatic entrance lens followed by a 150° spherical sector analyzer at an angle Ψ with respect to the surface. In most measurements we chose $\Theta + \Psi = 90^\circ$. As Ψ approaches 0° in Fig. 1(b), the path length inside the solid for electrons which are emitted below the surface drastically increases such that the detection of above or near surface emission is clearly favored. Due to the chamber alignment and the large acceptance angle of $\eta = 16 \pm 6^\circ$ of our electron spectrometer entrance lens, below-surface emission is always observed, but to a much smaller extent than

above or near surface emission. The absolute spectral intensity in the ($\Psi \simeq 0^\circ$)-geometries greatly diminishes, though. By rotating the target of Fig. 1(a) around the ion beam axis with the surface normal pointing out of the image plane, the condition of $\Theta + \Psi = 90^\circ$ could be relaxed, and geometries with $\Theta = 5^\circ$ and $\Psi = 0^\circ$ have been achieved.

The effective incident energy of the ions on the surface is given by E_{kin} plus the energy gain resulting from the image charge acceleration [24]

$$E_{\text{im}} \simeq \frac{W}{3\sqrt{2}}q^{3/2} \quad (1)$$

where the work function W equals 4.6eV for our Si target and $q = 9$. Accordingly, there will always remain a minimum incident energy of approx. 29eV leading to an additional perpendicular projectile velocity component $\Delta v_\perp = \sqrt{2 \cdot E_{\text{im}}/m}$. Thus the interaction period of the ion in front of the surface can principally not be stretched above an upper limit depending on q and W even though the original perpendicular velocity component $v_\perp = \sqrt{2E_{\text{kin}}/m} \cdot \cos(\Theta)$ of the projectile may vanish by selecting $U_Q = -U_P$ or $\Theta \mapsto 0^\circ$.

When the incident energy E_{kin} is lowered the beam spreads up at the target (Liouville's theorem) and incident angles may deviate from their nominal values Θ . In the energy domain $E_{\text{kin}} < E_{\text{im}}$, the projectile path is strongly bent by the attractive image acceleration causing increased effective incident angles Θ_{eff} , especially for small Θ . Hence the values given for Θ in this paper are intended to delineate the chamber geometry rather than the effective scattering geometry of an individual projectile.

Projectile penetration depths at the stage of complete neutralization and deexcitation can be estimated by multiplying v_\perp by a typical overall interaction time of 10^{-14} s. With $E_\perp = \frac{1}{2}mv_\perp^2$ expressed in eV, the perpendicular path length z_{pen} of the Ar projectile within the bulk can be attained from $z_{\text{pen}} = 0.22\text{\AA} \times \sqrt{E_\perp[\text{eV}]}$. This implies that at energies E_\perp in the range of 100eV, z_{pen} stays below one lattice constant amounting to 5.43\AA for Si. TRIM simulations [25] performed for a 10eV and a 100eV Ar¹⁺ beam impinging on a Si crystal at perpendicular incidence yield average lateral ranges of $3 \pm 1\text{\AA}$ and $10 \pm 4\text{\AA}$, respectively. These distances refer to the total penetration depth until the ion is stopped within the bulk.

III. EXPERIMENTAL OBSERVATIONS

Using the apparatus described in the preceding section, we have measured secondary electron spectra emitted by Ar^{9+} and metastable Ar^{8+} ions during their interaction with the Si wafer. In this work we will focus on examining the well defined high-energy L -Auger peaks covering the interval between 120eV and 300eV. The spectra also feature a low-energy part which extends up to more than 100eV. The analysis of electron spectra in this energy domain is aggravated by a lack of substructures, the superposition of kinetic and intra-atomic emission and their sensitivity to stray electromagnetic fields. Regarding the high-energy branch, we point out that no background due to kinetic electron emission has to be considered for $E_{\text{kin}} \leq 121$ eV since the collision energies $E_{\text{coll}} = E_{\text{kin}} + E_{\text{im}}$ are smaller than the lower bound of the spectral region to be examined. By selecting $U_Q = -20\text{V} < U_P = 12 \pm 2\text{V}$, we can prevent HCIs from reaching the grounded target. Only projectiles that are partially neutralized before the deceleration stages and secondary electrons which are generated by collisions of the HCIs with beam transport lens elements (these are on negative potentials) can hit the target where they may set free secondary electrons. We discovered that both contributions are negligible.

In Fig. 2 we present three Ar^{9+} spectra measured under $\Theta = 45^\circ$ and with $E_{\text{kin}} = 9$ eV, 121eV and 1953eV. This and all following spectra are normalized to the total intensity in the L -Auger region between 160eV and 240eV. Considering that at maximum one L -Auger process per ion takes place, this type of normalization method is suitable to display the intensity shifts between L -transition subgroups as discussed in this paper. We note that the calibration of the spectra to the absolute beam intensity is prone to errors which emerge from the uncertainty in the correction factors compensating geometrical and kinetic effects.

At first we recognize the general shape of an Ar^{9+} LMM spectrum featuring a dominant peak at 211eV, a broad structure reaching down to about 120eV on the low-energy side and a shoulder sitting on the high energy tail of the spectrum. At $E_{\text{kin}} = 9$ eV, this shoulder can be resolved into two subpeaks of almost equal height at 224eV and 232eV. Proceeding

to higher E_{kin} , the 232eV-peak disappears and the 224eV-peak gains intensity. Presumably due to the poor statistical quality, the latter 232eV-substructure cannot unambiguously be identified in de Zwarts [18] measurement¹ which was taken under the same experimental geometry and roughly the same incident energy on a tungsten target.

The data acquisition statistics of our spectra exhibits a remarkably high quality. Beam current shifts during measurements are compensated by an online normalization of the spectra to the overall charge current I_q hitting the target. The accumulated counts per 1eV energy channel in the ($\Theta = 45^\circ, E_{\text{kin}} = 121 \text{ eV}$)-spectrum amount to more than 200,000 at the 211eV-maximum letting the relative error drop below 0.3%. We note that each spectrum in Fig. 2 has been recorded in a single five minute run. This is possible due to the high current $I_q = 125\text{nA}$ on the target which can be converted into a particle current I_p by dividing I_q over the projectile charge q and applying a correction factor compensating secondary electron emission. Multiplying I_p by an appropriate geometrical factor, it can be shown that the overall experimental count rate in the high-energy branch roughly correlates to the emission of one high-energy electron per incoming HCl.

The spectral series of Ar^{9+} ions impinging on Si(100) with constant $E_{\text{kin}} = 121 \text{ eV}$ in Fig. 3 displays the variation of the relative peak intensities with the experimental geometry. Recalling Fig. 2, we discover that the presence of a strong 232eV-subpeak is connected to minimum perpendicular velocities v_\perp . In the measurement under $\Theta = 90^\circ$, the observation angle Ψ is very flat and a second broad peak region evolves around 198eV. Switching to the other “grazing observation” alignment at $\Theta = 5^\circ, \Psi = 0^\circ$, this structure is preserved proving that its presence is related to a small observation angle Ψ rather than the direction of incidence Θ or Θ_{eff} .

Under $\Theta = 5^\circ$, the perpendicular projectile penetration into the bulk is principally

¹There has obviously been a mistake in the calibration of the plot on the energy axis that has been corrected in [17].

limited to less than one lattice constant. The severe discrepancy between the two spectra under $\Theta = 5^\circ$ and $\Theta = 5^\circ, \Psi = 0^\circ$ in Fig. 3 illustrates the extreme above-surface sensitivity of the ($\Psi = 0^\circ$)-measurements since the physics of interaction is only determined by Θ_{eff} and E_{kin} which remain constant. We deduce that the broad peak region is generated above or at least near the first bulk layer. Because this region loses its weight under $\Psi = 45^\circ$ when electrons originating from all interaction phases are detected, above-surface processes only supply a minor fraction of the total high-energy emission. Nevertheless, the ratio between the *detected* above- and below-surface emission is strongly enhanced at grazing observation $\Psi = 0^\circ$ and small projectile penetration depths.

To obtain a quantitative estimate, we ran TRIM calculations [25] for Ar^{1+} ions colliding with a Si target. The results show that a few percent of the incoming particles are reflected for $E_{\text{kin}} = 121$ eV and 2 keV complying with the preceding interpretation of the ($\Psi = 0^\circ$)-spectra. We point out that one has to be careful about adopting these findings for HCI beams because the TRIM code solely employs potentials which are strictly speaking only valid for onefold ionized ground state projectiles. For incident energies of less than 10eV when $E_{\text{im}} > E_{\text{kin}}$, the code fails to produce physically meaningful output since it obviously misrepresents the potentials evolving from the complex coupling of the HCI-surface system. These potentials are decisive for the calculation of the HCI trajectory along the prolonged interaction period in front of the surface and the reflection probability. At such low incident energies, no experimental data on reflection coefficients of Ar^{q+} impinging on Si(100) are available in the literature or refers to grazing incidence conditions where the physics of interaction is different despite the similar vertical velocity components. The detection of the unique peak profile at grazing observation combined with the oncoming discussion may be regarded as indirect experimental evidence for the existence of reflected projectiles.

The shifts of the upper edge of the 211eV-peak in Fig. 3 can consistently be explained by an enhanced below-surface damping of the emitted electrons at $\Theta = 90^\circ$ which is more effective than at $\Theta = 5^\circ, \Psi = 0^\circ$ due to the higher perpendicular velocity component v_\perp .

In Fig. 4 we show spectra of Ar^{9+} ions impinging on a n-Si(100) surface under different

incident angles with minimal kinetic energies, i.e., $E_{\text{kin}} = 9 \text{ eV}$. For $\Theta = 5^\circ$ and $\Theta = 45^\circ$, the spectra are nearly identical reflecting the fact that the self-image attraction is greater than the kinetic projectile energy so that the effective angle of incidence Θ_{eff} becomes almost independent of its original value Θ . While approaching perpendicular incidence, the same broad region between 160eV and 205eV as in Fig. 3 pops up again. For the two different ($\Psi = 0^\circ$)-geometries, the main peaks exhibit about the same height. Since v_\perp is minimal in all four spectra, the upper edge of the 211eV-peak remains sharp and does not shift to lower energies due to bulk damping as in Fig. 2. Even more, the high-energy branches above 211eV coincide almost perfectly. Keeping in mind our particular choice of normalization method and the minimum incident energy $E_{\text{kin}} = 9 \text{ eV}$, the latter feature suggests that the peak intensity within the high-energy tail region results from above-surface emission which is insensitive to bulk damping of the outgoing electrons.

In Fig. 5 we present another series of Ar^{9+} spectra taken at a fixed angle $\Theta = 90^\circ$ (i.e., $\Psi = 0^\circ$) for different incident energies E_{kin} . As the point of emissions moves deeper into the solid, below-surface contributions are successively filtered out by bulk damping. The double-peak profile transforms into a single unstructured maximum widening to the low-energy side as E_{kin} increases. The low-energy bounds of the 198eV maximum coincide at $E_{\text{kin}} = 9 \text{ eV}$ and 121eV. The spectrum measured at $E_{\text{kin}} = 121 \text{ eV}$ demonstrates that the appearance of the broad peak structure under $\Psi = 0^\circ$ and the 232eV-peak occurring solely at minimal v_\perp are obviously not immediately linked to each other.

The combined analysis of the spectra in Figs. 2-5 renders the following preliminary picture which will be supported by further evidence and simulations in the next sections. The dominant 211eV-peak originates from below-surface emission since its center moves downward, it broadens and its intensity decreases when long path length of the emitted electrons through the bulk to the spectrometer entrance can be assumed. Furthermore, it does not disappear with growing v_\perp . This also holds for the lower lying part of the spectrum. Two equally intense subpeaks on the high-energy shoulder exclusively appear when v_\perp is minimized. As v_\perp increases, the 224eV-peak gains intensity while the 232eV-

peak quickly vanishes. This behavior suggests a dependence of the 232eV-intensity on the above-surface interaction time even though the resulting emission process may occur after surface penetration.

The broad peak region between 160eV and 205eV under $\Psi = 0^\circ$ and $E_{\text{kin}} \leq 121$ eV represents near- or above-surface emission since the “detection window” is shallow and the chamber geometry favors detection of above-surface transitions at the same time. Subsurface contributions are shielded by bulk damping. For reasons that will be given in Section VII, it is likely that it is made up of a small fraction of above-surface emission from partially screened incoming or ionized reflected particles. The preceding experimental findings will play a crucial role in the conception of an interaction model in Section VI.

IV. ENERGETIC GROUPING OF ATOMIC *LMM* TRANSITIONS

In this section we will attribute some spectral features occurring in the energy range between 150eV and 300eV to distinct groups of *LMM* Auger transitions. The energetic overlap between neighboring groups will “fortunately” turn out to be sufficiently small such that relative peak intensities can be related to the participation of distinguished Auger processes. Furthermore, certain projectile deexcitation mechanisms can definitively be ruled out if no intensity is measured in their proper energy range. By merely comparing peak energies, we obtain valuable information concerning the HCl-solid interaction which supplement the experimental observations of Section III *before* launching any simulation. At the present state of research, peak energies can be evaluated more accurately than transition rates for the HCl solid system.

We employ the well known Cowan code [26] in order to simulate configuration energies based on spherically symmetrized wave functions for *free* atoms and ions. In order to calculate Auger transition energies *within the bulk*, we have to take into account the effect of the self induced charge cloud consisting of valence band (VB) electrons which surrounds the HCl. First approaches have been made on this behalf [13,27] using the density functional

theory (DFT). Results show that the nonlinear screening effects due to the electron gas are to a good approximation equivalent to the screening by outer shell “spectator” electrons in a free atom.

The hollow atom entering the bulk loses all Rydberg shell electrons due to the screening by the target electron gas. The radii of the resonantly populated orbitals are of the order of the capture distances, i.e., about 10\AA and therefore much larger than the Thomas-Fermi screening length of less than one Ångström as derived in a free electron gas model. Therefore all Rydberg levels will be depleted leaving behind the original $1s^22s^2p^5$ core configuration and possibly some M -, N - and O -shell electrons. The target electron gas will swiftly take over the role of the outer electrons to screen and so neutralize the HCI charge. A good estimate for the reaction rate of the electron gas to the HCI “point charge” perturbation is provided by the plasmon frequency which lies in the vicinity of 10^{16}s^{-1} for metals. This is way above typical rates of the other HCI bulk interaction processes and we can thus assume that the HCI core screening by VB electrons is instantaneous. Except for the special handling of the transitions with $3d$ participation, which will be outlined below, all subsurface Auger transition energies given in this paper will hence be derived for neutral initial states possessing a total amount of q M - and N -shell electrons and singly ionized final states.

Let us now look at the grouping of LMM transitions which is plotted in Fig. 6. The histogram displays the energetic positions of all LMM transitions originating from initial $2p^53s^x p^y d^z$ configurations ($n_M = x+y+z \leq 9$) of “hollow” Ar^{9+} atoms which are neutralized via $q - n_M$ “spectator” electrons in the N -shell. Angular momentum coupling as in [5] is not taken into account. Each transition is weighted by unity in the plot discarding transition rates and statistical factors due to different subshell occupations. For the sake of clarity, the whole spectrum is convoluted by a Gaussian function of constant width 2eV . This modification evens out conglomerations of Auger lines at certain energies which are an artifact of strictly applying the spectator electron approximation. The width is sufficiently small not to lead to an additional overlap of LMM subgroup intensities.

Within the same group, Auger transition energies generally tend to increase steadily

with the overall shell population. For comparison, the dotted line in Fig. 6 represents an autoionization spectrum of Ar^{9+} ions impinging on a $\text{Si}(100)$ surface at $E_{\text{kin}} = 121$ eV and $\Theta = \Psi = 45^\circ$ as reproduced from the experimental data in Fig. 2.

Fig. 6 reveals that *LMM* Auger transitions involving a free and initially neutral Ar atom can cover the energy interval between 166eV ($2p^5 3s^2 4s^2 p^5 \mapsto 2p^6 3s^0 4s^2 p^5$) and 267eV ($2p^5 3d^9 \mapsto 2p^6 3d^7$). For convenience, the groups of *LMM* transitions displayed in Fig. 6 and the following part of the paper are classified by the angular ℓ quantum numbers of two participating *M*-shell electrons. In all cases, the final states are made up of the atomic $2p$ level, the remaining *M*-core states and an appropriate continuum state. For *LMM* processes, we omit the $2p$ level in our notation.

The low-energy part of the *LMM* spectrum can be assigned to $3ss$ - and $3sp$ transitions. The higher $3sp$ intensity can be explained by their statistical weight and their $3p$ contribution clearly enhancing the transition rates. The fact that the two small peaks arising in some spectra between 190eV and 200eV fall into the $3sp$ peak region in Fig. 6 might be fortuitous. Due to our coarse resolution concerning the energetic grouping, we are not able to ascribe these peaks to particular $3sp$ transitions.

Several things indicate that the dominant peak region around 211eV is composed of $3pp$ transitions out of a massively occupied *M*-shell instead of $3sd$ transitions the energy range of which also covers this peak region. At first, it is intuitively plausible, considering that all three bound state wave functions possess the same angular momentum, that the by far highest *LMM* rates are calculated for the $3pp$ group. Second, the sharp upper edge of the 211eV-maximum resembles the upper boundary of the $3pp$ curve which is composed of $3pp$ transitions out of a completed *M*-shell. Due to level filling statistics, a sharp edge is unlikely to form if its corresponding transitions take place out of intermediate shell occupations. Third, atomic structure calculations yield that $3pp$ energies accumulate around 211eV for all initial $3s^2 p^y d^z$ configurations ($y + z \geq 5$), regardless of the particular choice of y and z . This automatically implies that prior to the majority of all $3pp$ decays either more than seven electrons have to be captured into the *M*-shell or the induced charge cloud provides

an equivalent screening effect.

According to the *LMM* grouping in Fig. 6 we can assign the two subpeaks on the high-energy shoulder of the *LMM*-maximum to *3sd*- and *3pd* transitions, respectively. *3pp* processes are unlikely to contribute to the region above 213eV since they require at least one *3s* vacancy along with a ninefold occupied *M*-shell. These initial configurations will immediately be converted into $3s^2$ configuration due to the very fast super Coster-Kronig (sCK) decay channel involving three *M*-shell electron levels.

The spectral range of the *3pd* peak is cut off at about 235eV and *3dd* transitions do obviously not produce enough intensity to appear with a distinct peak region in the spectra. These observations provide experimental evidence that the *3d* level cannot be completely populated within the bulk and that quick sCK transitions tend to carry *3d* populations into lower lying sublevels before *LMM* transitions take place. The missing structures and the spectral range of the high-energy tail extending above 300eV suggest that it consists of the large variety of *LXY* transitions with $X, Y \in \{N, O\}$ rather than *3dd* transitions.

The *LMM* cut-off at 235eV can be understood by taking a deeper look at the effective projectile potential V_{eff} within the bulk (see Fig. 7) which is deformed with respect to the corresponding free ionic Coulomb potential $V_{\text{Coul}}^{\text{free}}$. Close to the projectile nucleus $r \ll a_0$, the effective potential V_{eff} converges into $V_{\text{Coul}}^{\text{free}}$. At intermediate distances $r \simeq a_0$, the screening of outer levels and the electron gas starts to act on the projectile levels. In this domain V_{eff} is well represented by a free atom potential $V_{\text{Coul}}^{\text{screen}}$ which is screened by outer shell spectator electrons. All *nl* subshells with energies E_b^{nl} are elevated by a subshell dependent amount of ΔE_b^{nl} with respect to $V_{\text{Coul}}^{\text{free}}$. Far away from the nucleus the effective potential V_{eff} merges into V_0 denoting the bottom of the valence band.

Fig. 8 displays the *M*-sublevel binding energies E_b^{nl} of Ar^{9+} as a function of the total *M*-shell population n_M . The values have been calculated by the Cowan code for spectator electron configurations, i.e., for the potential $V_{\text{Coul}}^{\text{screen}}$. This modeling has proven to yield good agreement with experimental and more sophisticated theoretical results in the past. In a work by Schippers *et al.* [5], the main *KLL* peak energies of the hydrogenlike second

row ions C^{5+} , N^{6+} , O^{7+} , F^{8+} and Ne^{9+} have been reproduced. Arnau *et al.* [27] have demonstrated that the spectator electron model complies with DFT calculations including nonlinear screening effects for hydrogenlike Ne^{9+} ions in an Al target. Detailed calculations even reveal that the induced charge density tries to mimic the shape of the wavefunctions of the neighboring unoccupied atomic level.

In Fig. 8 we added $2p$ binding energies of hydrogenlike C^{5+} and Ne^{9+} as obtained from the spectator model and for comparison the DFT calculation for Ne^{9+} as a function of the total L -shell population n_L . Following [27], the screening of the atomic spectator electrons resembles the screening by the VB electron gas because the inner atomic levels are energetically separated from the VB much like they are separated from next higher subshell in a free atom. This argument holds for the Ar^{9+} $3s$ - and $3p$ level and also for nearly all L -shell levels in hydrogenlike HCIs which are situated between the C^{5+} and Ne^{9+} curves.

The evolution of the $3d$ sublevel energies with n_M in Fig. 8 differs from the lower lying subshells, though. We observe that the $3d$ level binding energies are significantly closer to the VB and grow above V_0 as soon as more than five electrons populate the M -shell. We performed a DFT calculation showing that $3d$ electrons are already lost to the VB continuum for $n_M > 4$. The spectral cut-off in the $3pd$ transition domain in Fig. 6 can now be explained by omitting all contributions from $3pd$ transitions with $n_M > 4$. Aiming to correct for the shape of V_{eff} which largely deviates from $V_{\text{Coul}}^{\text{screen}}$ for $E_b^{nl} \simeq V_0$ (see Figs. 7 and 8), we shift the atomic $3d$ level to V_0 for $n_M \leq 4$ to attain higher transition energies compared to the mere spectator electron model. In this manner we derive the experimental $3sd$ - and $3pd$ peak positions on the high-energy shoulder within an accuracy of 2% and 1%, respectively.

V. MONTE CARLO SIMULATION OF THE SUBSURFACE INTERACTION PHASE

In order to elucidate the interaction mechanism which eventually generates the measured spectra we worked out a Monte Carlo simulation [28]. Our goal was to reproduce the intensity

shifts of the observed spectra for different incident energies in Fig. 2. On the analogy of previous simulations by Schippers et al. [5], Page et al. [10] and Stolterfoht et al. [11] on the L -shell filling of hydrogenlike highly charged ions at metal surfaces, we only keep track of the populations of the two innermost projectile shells containing at least one vacancy and focus on the most dominant transition rates. The ionic cores are neutralized by N -shell spectator electrons. Among all intra-atomic Auger processes, only those yielding an electron above the vacuum level are considered.

During the simulation, the three M -subshell populations are recorded continuously. Transition rates, transition energies and sublevel energies are evaluated dynamically at each iteration step according to the particular $\{n_{3s}|n_{3p}|n_{3d}\}$ configuration. From one step to the next, only the fastest transition which is derived statistically from its nominal rate takes place. The Monte Carlo method implies the averaging of the simulation results over a sufficient amount of projectiles. We find that the simulated spectra converge after $N \simeq 1 \times 10^5$ particle runs and chose $N = 1 \times 10^6$. In our implementation of the subsurface cascade, each particle is started at the first bulk layer with a fixed angle of incidence $\Theta = 45^\circ$ and energy E_{kin} . For $E_{\text{kin}} = 121$ eV and 2 keV we assume an initially empty M -shell.

A. Intra-Atomic rates

The LMM rates are evaluated by a fit expression proposed by Larkins [29] for free multiply ionized atoms possessing no N -shell spectator electrons. Accordingly, if one or two of the n electrons of a subshell which could contain n_0 electrons are involved in an Auger process, the Auger rate calculated using the formulae appropriate for a filled shell $\Gamma_{\ell_1\ell_2}^{\text{filled}}$ is reduced by n/n_0 or $[n(n-1)]/[n_0(n_0-1)]$, respectively. Values for $\Gamma_{\ell_1\ell_2}^{\text{filled}}$ are only supplied for $3ss$ -, $3sp$ - and $3pp$ transitions in the literature which account for the greatest part of the overall LMM intensity in the literature. For $3sd$ -, $3pd$ - and $3dd$ transitions, we scale the LMM rates $\Gamma_{3ld}^{\text{filled}}$ to reproduce the experimental peak heights. Table I lists the six $\Gamma_{\ell_1\ell_2}^{\text{filled}}$ rates which are held constant for different simulations.

These *LMM* rates should not be greatly affected by the embedding of the HCI into the electron gas because they chiefly depend on the radii of the participating *M*-subshells which remain fairly unchanged. To show this we recall that the shape of the induced charge cloud is similar to the *N*-shell. Within the hydrogen atom approximation, the radii of the screening cloud r_{sc} and the atomic shells (schematically inserted in Fig. 7) both scale with $(n-1)^2\{1+\frac{1}{2}[1-\frac{\ell(\ell+1)}{(n-1)^2}]\}$. The ratio $r_{sc}/r_{3p} = 2.5$ with $sc = 4p$ has to be related to the ratio r_{3p}/r_{3s} amounting to 0.83. Due to its great extension, the screening electron cloud should therefore have a minor impact on the *M*-shell orbitals and hence on the *LMM* rates given in Table I.

Since we do not resolve *N*-sublevels, Coster-Kronig *MMN* transitions have to be handled by a global base rate for each *M*-level pair. In a simple approach, we weight each *MMN* base rate by the initial *M*-sublevel occupation and final state vacancies such that the average rate amounts to $3 \times 10^{14} \text{s}^{-1}$. For the purposes of this paper, only the order of magnitude with respect to the other transition types matters. We remark that Armen and Larkins [30] have calculated transition rates for *MMN* decay channels which are of the order of $4 \times 10^{14} \text{s}^{-1}$, depending strongly on the angular coupling. This is in sufficiently good agreement with our assumption. Only *MMN* transitions with a final state above the continuum level are included leaving over solely $(3s)(3d)N$ transitions which are of particular importance for the initial phase of the interaction.

The sCK *MMM* rates are known to be 10 to 100 times faster than any rates for Auger transitions possessing the initial and final holes in different principal shells. In our simulation, they mainly serve to regroup any *M*-shell configuration into the appropriate *M*-shell ground state before *LMM* transitions take place. To achieve this, we utilize a base rate of $1 \times 10^{15} \text{s}^{-1}$ which is scaled by the *M*-subshell occupation statistics. In Table II we put together the average number of *MMM* processes per particle and the average *M*-sublevel occupation at the time of *MMM* emission for the two sCK transitions which are relevant for our simulation.

B. *MCV filling within the bulk*

Target levels below V_0 can be filled by transitions involving electrons of valence band states (C) which are perturbed by the ionic core. The energy gain is conveyed either onto another VB electron which is emitted into the continuum or a collective excitation (plasmon) is created in the medium. The theoretical approach including the charge displacement in the description of the excited outgoing electrons is much more complicated and, at present, only unperturbed valence band states (V) are included in the calculations [14,15]. The VB electrons take on the role of outer shells in a free atom.

Using DFT to describe the interaction between the ion and the metal valence band and following the same scheme as in [15], we have derived *MCV* rates for the Ar^{9+} -Si system. Table III lists the rates per spin state $\Gamma_{3\ell}^{MCV}$ into the three *M*-sublevels with the number of initial *M*-shell electrons n_M as parameter. These *MCV* rates still have to be multiplied by the number of unoccupied final states in the particular *M*-sublevel to attain actual transition rates between two atomic configurations. Γ_{tot}^{MCV} denotes the overall *MCV* rate into the *M*-shell after carrying out the appropriate statistics. Since sCK transitions are much faster than *MCVs* (cf. Table II), we only consider ‘‘Coster-Kronig final states’’ as initial configurations in the DFT calculation. The transition rates are independent of the projectile velocity v_p equaling their static values for all incident energies occurring in this work.

Table III reveals that Γ_{3d}^{MCV} assumes by far the highest values. Taking into account the high degeneracy of the *3d* level, effective rates Γ_{3d}^{MCV} exceed Γ_{3p}^{MCV} and Γ_{3s}^{MCV} by more than one and two orders of magnitude, respectively. With increasing n_M , *MCV* transfer into the *3p* state accelerates reaching the Γ_{3d}^{MCV} values at low n_M . This is important considering that for $n_M > 4$ the *3d* shell vanishes and *MCVs* into the *3p* level constitute the most effective *M*-shell filling mechanism which is eventually responsible for the formation of the dominant 211eV-peak.

C. Collisional filling

For projectile energies above 1 keV, sidefeeding into the HCI M -shell due to direct electron transfer from target atom core levels supplies a velocity dependent filling rate. The transfer crosssection increases with the energetic vicinity of inner projectile and target states [31] which is maximum for the Ar^{9+} $3s$ level with the $2p$ bulk level of Si possessing $E_b^{2p} = 109$ eV (cf. Fig 8). Experimentally, a Si target LMM Auger peak for spectra with $E_{\text{kin}} \geq 1$ keV can be observed which is directly connected to the vacancy transfer. For 2 keV projectiles traveling through a silicon crystal in (100)-direction, collisional filling supplies a $3s$ sidefeeding rate of $\Gamma_{3s}^{\text{coll}} = v_p/d = 1.8 \times 10^{14} \text{s}^{-1}$ going on the assumption of one electron transfer per collision. Within the energy range below 1 keV, collision frequencies are small and the distance of closest approach is too large even for head-on collisions to allow a sufficient level crossing for sidefeeding [31].

D. Simulation of the 121eV- and 2 keV-spectra

In Fig. 9 we plot the experimental spectra from Fig. 2 into three subplots and compare them with our simulation results which are convoluted by a Gaussian function of 3eV width. In this section we look at the Ar^{9+} spectra and postpone the discussion of the Ar^{8+} spectra which are displayed in the same plot to Section VII. The difference between the simulated spectra in (a) and (b) stems from collisional filling which is exclusively enabled for $E_{\text{kin}} = 2$ keV. In addition, we performed a convolution of the 2 keV-spectrum with an exponential function with a decay length of 3 a.u. to compensate for elastic and inelastic energy losses of electrons on their way through the bulk region. For $E_{\text{kin}} < 2$ keV, this damping becomes negligible due to the shallow projectile penetration.

The intensity ratios among the different LMM subgroups and their peak positions are approximately reproduced. The $3pp$ region displays too much intensity, though which might be caused by the LMM rate fit formula (cf. Section V A) overestimating the $3pp$ rates for

high M -populations, see also [29] (Table VI). The $3ss$ intensity is clearly too low suggesting that other transition types not considered in our model may contribute to this region. The enhancement of the $3sd$ peak parallel to the disappearance of the $3pd$ peak and intensity gain of the $3sp$ region towards the $E_{\text{kin}} = 2$ keV-spectrum as a consequence of the collisional filling can nicely be observed (cf. Table I). The average M -sublevel populations at the time of LMM emission (cf. Table I) indicate that the high-energy shoulder is generated along the early subsurface interaction phase. On the other hand, the dominant $3pp$ peak occurs at high M -populations benefitting from the growing MCV rates into the $3p$ level and the disappearance of the $3d$ level towards high n_M . The missing $3dd$ intensity confirms the presence of the fast MMN and MMM decay channels which inhibit the buildup of $3d$ populations larger than one.

In the experimental spectra, the low-energy tail displays much less structure than the simulation indicating that the mere spectator electron model might be incomplete. We carried out other simulations where 20% of the LMM transitions start out from singly ionized initial configurations such that the peak regions lose part of their intensity to the low-energy side. Doing so the intensity dip around 200eV gets partially ironed out and the low-energy tail stretches beyond 160eV. A similar effect could be induced by the consideration of $L_{2,3}MMM$ double Auger processes [32] for which Carlson and Krause [33] measured a relative contribution to all radiationless transitions of $10\pm 2\%$ and energy shifts of more than 10eV [34]. For the sake of the clarity of the displayed simulation results we did not implement this correction in Fig. 9.

E. Simulation for a statistical initial M -population

It is very surprising that by reducing the incident energy from about 121eV to 9eV, a significant shift in the relative peak intensities still takes place. On the one hand velocity dependent below-surface filling can be ruled out in this energy domain, on the other hand this effect must originate from different subshell populations at the time of LMM emission. Let

us assume for the moment that individual M -subshells of each particle are filled statistically (by a Poisson distribution which is cut off at the subshell degeneracy) at the first bulk layer according to their respective degeneracy, i.e., $\langle n_{3\ell} \rangle = 2/18, 6/18$ and $10/18$, multiplied by the mean total M -shell population $\langle n_M \rangle$ for $\ell = 3s-, 3p-$ and $3d$ level, respectively. In Fig. 9 we present results of a Monte Carlo simulation with $\langle n_M \rangle = 2$.

For a greater part of these initial configurations, new M -shell redistribution channels open up via $MMNs$ and $sCKs$ which are energetically forbidden for $n_M = 0$ and carry part of the $3d$ population immediately into the $3p-$ rather than the $3s$ level. The simulations in Fig. 9(b,c) and Table I indeed reproduce the intensity shift from the $3sd$ peak to the $3pd$ peak at 232eV going from $E_{\text{kin}} = 121\text{eV}$ to 9eV. We remark that this simple model of an initial M -shell population before bulk penetration does not hold exactly for the Ar^{8+} simulation where we set $n_{3s} = 1, \langle n_{3p} \rangle = 1$ and $\langle n_{3d} \rangle = 1$. We are going to provide a physical motivation for the model in Section VII.

VI. THE EVOLUTION OF THE SUBSURFACE CASCADE

According to the experimental clues and arguments of Sections III and IV, the overwhelming part of the high-energy branch originates from below-surface emission. For this phase, we designed the simulation presented in the previous section. In the following we describe the evolution of the subsurface cascade on the basis of the simulation results combined with the experimental data.

As the HCI penetrates into the crystal bulk region all electrons that have previously been captured into outer Rydberg levels will be lost and band electrons will neutralize the core charge over a distance of roughly the Debye screening length of the electron gas. Thus a second generation of hollow atoms emerges within the bulk.

Prior to any electron capture, the O -shell of the Ar^{9+} core is the uppermost ionic shell to still fit below V_0 . As long as not more than two electrons populate inner levels, solely XCV transitions (with $X \in \{L, M, N, O\}$) can proceed. Since the XCV transition probability

increases with the effective screening and degeneracy of the final level, XCVs preferably populate the O -shell. Before any significant NOO and MNO Auger emission can take place, the rapid XCV filling successively pushes the O - and N -shell above V_0 . This period is accompanied by LCV, LNO, LMN transitions etc. creating the smoothly decreasing part of the spectrum above the $3pd$ edge. We note that this early phase of the neutralization may already start before complete bulk penetration when the projectile travels through the vacuum tail of the valence band.

The loss of whole atomic shells into the valence band stops when the M -shell is reached. At this point of the scenario, a low M -shell population with a statistical preference for the $3d$ level (due to its high degeneracy) is likely to occur. MMN -CK processes transfer these $3d$ electrons quickly into the $3s$ level before a large $3d$ population can accumulate. Other MMN transitions $(3p)(3d)N$ and later $(3s)(3p)N$ are energetically forbidden. This M -shell redistribution is accelerated by high speed sCK processes with rates of the order of 10^{15}s^{-1} . Whereas $3sdd$ transitions are immediately possible, MMM transitions into the $3p$ level require $n_M > 3$. Along this early M -shell redistribution phase the M -population remains fairly constant at $n_M \simeq 2 + n_{3s}$, though because one M -electron is lost along each MMM process. Thus $3sd$ - LMM processes out of initial $3s^2d$ constellations are characteristic for this phase causing the 224eV-peak in the experimental spectra. It lasts comparatively long because the condition $n_M \simeq 2$ keeps the MCV rates (cf. Table III) minimal.

The Ar^{9+} core will always be surrounded by an induced VB charge cloud (C) because the number of bound states n_b below V_0 is smaller than the projectile core charge $q = 9$ (Fig. 8). Hence MCV processes continue to populate empty M -levels faster and faster with increasing n_M . As soon as $n_M > 3$ is satisfied, $3pdd$ sCKs become energetically possible and a $3p$ population builds up while the $3d$ population remains approximately at one due to the presence of the MMN and sCK decay channels. $3dd$ transitions require the transient formation of very unstable M -shell configuration that are unlikely to occur so they do not appear in the spectra. At $n_M > 4$, the $3d$ level vanishes into the valence band thus interrupting further $3sd$ - and $3pd$ emission. Since the $3pp$ - LMM transitions possess much

higher rates than any other *LMM* transitions they clearly prevail during this later stage of the subsurface interaction.

The dominant peak which is centered at 211eV for $E_{\text{kin}} \leq 121$ eV in Fig. 2 corresponding to *3pp* transitions with $n_M \geq 7$ provides evidence for the described mechanism, in particular for the high *MCV* rates into the *3d*- and later the *3p* level. The intensity gain of the *3sd* peak with respect to the *3pd* peak for high E_{kin} is consistent with the greater time window of the former transition during the early interaction phase. This effect furthermore verifies the assumption of collisional sidefeeding into the *3s* level and therefore the 224eV-peak assignment by itself. All phases are accompanied by *3ss*- and *3sp-LMM* transitions which constitute the low-energy tail and the region around the two faint subpeaks between about 180eV and 200eV, respectively.

VII. SPECTRA OF METASTABLE Ar^{8+} PROJECTILES

Seeking to extract additional experimental evidence for the described Ar^{9+} interaction mechanism, we performed a series of measurements involving metastable ($2p^53s$) Ar^{8+} ions colliding at $\Theta = 45^\circ$ and various kinetic energies with a Si crystal (Fig. 10). A straight comparison with the corresponding Ar^{9+} series in Fig. 2 shows that the general shape of the spectra is unaffected by the additional *3s* electron except for a slight enhancement of the *3ss*- and *3sp* intensities. In fact, the only new structure observed is a small peak arising at 247eV for $E_{\text{kin}} = 8$ eV and generally for lowest perpendicular projectile velocities v_\perp which can also be deduced from Fig. 11.

The 247eV-peak has been discussed in detail in [35] along with corresponding peaks which occur under similar conditions in the spectra of second row ions in *1s2s* configurations. It can be assigned to so called *LMV_W* transitions in the course of which the *3s* electron jumps into the *2p* vacancy. The emitted electron comes from a level possessing a binding energy which equals the target work function $W = 4.6$ eV for silicon. Due to the shape of the subsurface potential V_{eff} (Fig. 7), these levels cannot exist after projectile penetration into the bulk

occurred. As mentioned earlier in Section IV, the strong decrease in spectral intensity above 235eV gives evidence for this assertion.

The identification of an above-surface LMV_W peak suggests that inner atomic shells $X \in \{M, N, O, \dots\}$ could be partially filled before bulk penetration by an autoionization process XV_WV_W . We mentioned earlier that also MCV set in with continuously increasing rates as the HCI travels through the vacuum tail of the valence band. Compared to the MCV filling within the bulk, these near-surface M -shell filling channels are likely to proceed significantly slower, though. Since sCK processes require certain minimum M -shell populations they are widely inhibited for these constellations. One can thus expect that a very slow projectile might enter the bulk region with a low M -shell population $\langle n_M \rangle \simeq 2$ favoring the $3d$ level due to its degeneracy. This way we can motivate the ansatz for the simulation of the spectra at minimum E_{kin} in Section V E, even though an explicit experimental evidence is still missing.

The astonishing similarity of the rest of the Ar^{8+} and the Ar^{9+} data bears out our previous assumption of fast MCV , MMN and sCK processes within the bulk redistributing any M -shell population swiftly into the $3s$ level. In order to compensate for the additional $3s$ electron in Ar^{8+} M -shell, sCKs have to proceed before an LMM transition takes place. This automatically implies that the M -shell must be sufficiently populated and quickly replenished at this point. Because a large M -shell population far in front of the surface would be in contradiction to all previous experiments we can exempt the above-surface zone as the origin of the emitted electrons. This obviously also holds for the $3pd$ peak at 232eV.

We made use of the great correspondence of the Ar^{8+} and the Ar^{9+} spectra to check the mechanisms and rates entering our interaction model. For the simulations on Ar^{8+} projectiles which are also shown in Fig. 9 we kept the same transitions types and rates but added an $3s$ electron to the initial M -shell population. Within the accuracy of our interaction model, the similarity of the two series is well reproduced.

VIII. SUMMARY AND DISCUSSION

In this work we have presented detailed experimental results on the interaction of Ar^{9+} and metastable Ar^{8+} ions impinging on a Si(100) crystal. Doing so we focused on autoionization spectra measured at low impact energies. In this energy domain, we identified several new spectral features which alter with the perpendicular projectile velocity component and with the angle of incidence and observation. A consistent interaction model has been suggested for which *MCV* processes and the energetic vicinity of the Ar^{9+} $3d$ subshell to the bottom of the silicon valence band play a decisive role.

The subsurface interaction phase has been simulated using a Monte Carlo code. Feeding the code with realistic transition rates, we have been able to reconstruct the experimental peak positions and intensity shifts for different projectile energies. Our results give indirect evidence for a very effective below-surface *MCV* filling as postulated by theory. In contrast to *KLL* spectra of hydrogenlike second row ions impinging on metal surfaces, the main intensity of the Ar^{9+} *LMM* spectra is located on the high-energy side of the peak region corresponding to a massively occupied $3p$ subshell. We demonstrated that this peculiar shape of the high-energy region is linked to the special role of the $3d$ subshell which mediates a fast *M*-shell filling in the beginning and later disappears due to the screening of the valence band electron gas.

We presented spectra measured at small observation angles with respect to the surface parallel. They contain a high intensity peak region which most likely originates from Auger emission of incoming or reflected projectiles which do not experience the full bulk screening, yet. In addition, we spotted a distinct peak in the Ar^{8+} spectra for the lowest perpendicular incident velocities which can be explained by a unique above-surface process involving the *L*-vacancy and two electrons from the resonantly populated shells.

HCI beams have been deemed a candidate for future surface modification techniques for some time. It has been demonstrated that single ions can give rise to nanoscale size features on certain surfaces [36]. Also sputter yields on insulators could be significantly enhanced by

using slow HCIs instead of fast singly charged projectiles. At very low kinetic energies, the energy deposition concentrates on a very small area which extends approximately one lattice constant in the vicinity of the first bulk layer. In this manner, an energy of several keV can be carried into this zone where it might be converted into activation energy for processes like sputtering, crystal growth and surface catalysis. Research in this field is under way and first results have been presented already.

ACKNOWLEDGMENTS

This work was sponsored by the German Bundesministerium für Bildung, Wissenschaft, Forschung und Technologie under Contract No. 13N6776/4. We are also grateful for support from the Ministerium für Wissenschaft und Forschung des Landes Nordrhein-Westfalen.

REFERENCES

- [1] J. Burgdörfer, P. Lerner, and F. W. Meyer, *Phys. Rev. A* **44**, 5674 (1991).
- [2] J. Ducrée, F. Casali, and U. Thumm, accepted by *Phys. Rev. A* (1998).
- [3] F. W. Meyer, L. Folkerts, H. O. Folkerts, and S. Schippers, *Nucl. Instrum. Methods Phys. Res., Sect. B* **98**, 441 (1995).
- [4] S. Hatke, A. Hoffknecht, S. Hustedt, J. Limburg, I. G. Hughes, R. Hoekstra, W. Heiland, and R. Morgenstern, *Nucl. Instrum. Methods Phys. Res., Sect. B* **115**, 165 (1996).
- [5] S. Schippers, J. Limburg, J. Das, R. Hoekstra, and R. Morgenstern, *Phys. Rev. A* **50**, 540 (1994).
- [6] F. W. Meyer, S. H. Overbury, C. D. Havener, P. A. Zeijlmans van Emmichoven, and D. M. Zehner, *Phys. Rev. Lett.* **67**, 723 (1991).
- [7] R. Köhrbrück, M. Grether, A. Spieler, N. Stolterfoht, R. Page, A. Saal, and J. Bleck-Neuhaus, *Phys. Rev. A* **50**, 1429 (1994).
- [8] S. Hustedt, J. Freese, S. Mähl, W. Heiland, S. Schippers, J. Bleck-Neuhaus, M. Grether, R. Köhrbrück, and N. Stolterfoht, *Phys. Rev. A* **50**, 4993 (1994).
- [9] J. Limburg, S. Schippers, I. Hughes, R. Hoekstra, R. Morgenstern, S. Hustedt, N. Hatke, and W. Heiland, *Nucl. Instrum. Methods Phys. Res., Sect. B* **98**, 436 (1995).
- [10] R. Page, A. Saal, J. Thomaschewski, L. Aberle, J. Bleck-Neuhaus, R. Köhrbrück, M. Grether, and N. Stolterfoht, *Phys. Rev. A* **52**, 1344 (1995).
- [11] N. Stolterfoht, A. Arnau, M. Grether, R. Köhrbrück, A. Spieler, R. Page, A. Saal, J. Thomaschewski, and J. Bleck-Neuhaus, *Phys. Rev. A* **52**, 445 (1995).
- [12] J. Limburg, S. Schippers, R. Hoekstra, R. Morgenstern, H. Kurz, M. Vana, F. Aumayr, and H. Winter, *Nucl. Instrum. Methods Phys. Res., Sect. B* **115**, 237 (1996).

- [13] A. Arnau, P. A. Zeijlmans van Emmichoven, J. I. Juaristi, and E. Zaremba, Nucl. Instrum. Methods Phys. Res., Sect. B **100**, 279 (1995).
- [14] R. Díez Muiño, A. Arnau, and P. M. Echenique, Nucl. Instrum. Methods Phys. Res., Sect. B **98**, 420 (1995).
- [15] R. Díez Muiño, N. Stolterfoht, A. Arnau, A. Salin, and P. M. Echenique, Phys. Rev. Lett. **76**, 4636 (1996).
- [16] S. T. de Zwart, Nucl. Instrum. Methods Phys. Res., Sect. B **23**, 239 (1987).
- [17] L. Folkerts and R. Morgenstern, Journal de Physique **Colloque C1**, suppl. no 1, 541 (1989).
- [18] S. T. de Zwart, A. G. Drentje, A. L. Boers, and R. Morgenstern, Surf. Sci. **217**, 298 (1989).
- [19] H. J. Andrä, A. Simionovici, T. Lamy, A. Brenac, G. Lamboley, S. Andriamonje, J. J. Bonnet, A. Fleury, M. Bonnefoy, M. Chassevent, and A. Pesnelle, Z. Phys. D **21**, suppl., 135 (1991).
- [20] R. Köhrbrück, K. Sommer, J. P. Biersack, J. Bleck-Neuhaus, S. Schippers, P. Ronci, D. Lecler, F. Fremont, and N. Stolterfoht, Phys. Rev. A **45**, 4653 (1992).
- [21] H. J. Andrä, A. Simionovici, T. Lamy, A. Brenac, and A. Pesnelle, Europhys. Lett. **23**, 361 (1993).
- [22] L. Folkerts and R. Morgenstern, Europhys. Lett. **13**, 377 (1990).
- [23] J. Limburg, J. Das, S. Schippers, R. Hoekstra, and R. Morgenstern, Phys. Rev. Lett. **73**, 786 (1994).
- [24] H. Winter, C. Auth, R. Schuch, and E. Beebe, Phys. Rev. Lett. **71**, 1939 (1993).
- [25] J. F. Ziegler, J. P. Biersack, and U. Littmark, in *The Stopping and Range of Ions in*

- Solids*, edited by J. F. Ziegler (Pergamon Press, New York, 1985), Vol. 1.
- [26] R. D. Cowan, *The Theory of Atomic Structure and Spectra* (University of California Press, Berkeley, 1981).
- [27] A. Arnau, R. Köhrbrück, M. Grether, A. Spieler, and N. Stolterfoht, *Phys. Rev. A* **51**, R3399 (1995).
- [28] M. H. Kalos and P. A. Whitlock, *Monte Carlo Methods* (John Wiley & Sons, New York, 1986), Vol. I: Basics.
- [29] F. P. Larkins, *J. Phys. B* **4**, L29 (1971).
- [30] G. B. Armen and F. P. Larkins, *J. Phys. B* **24**, 741 (1991).
- [31] M. Grether, A. Spieler, R. Köhrbrück, and N. Stolterfoht, *Phys. Rev. A* **52**, 426 (1995).
- [32] T. Åberg, in *Atomic Inner-Shell Processes I: Ionization and Transition Probabilities*, edited by B. Crasemann (Academic Press, New York, 1975), Chap. 9, pp. 353-375.
- [33] T. A. Carlson and M. O. Krause, *Bull. Amer. Phys. Soc.* **10**, 455 (1965).
- [34] K. Siegbahn, C. Nordling, A. Fahlman, R. Nordberg, K. Hamrin, J. Hedman, G. Johansson, T. Bergmark, L. O. Werme, R. Manne, and Y. Baer, *ESCA Applied to Free Molecules* (North-Holland, Amsterdam, 1969).
- [35] J. Ducrée, J. Mrogenda, E. Reckels, M. Rütter, A. Heinen, Ch. Vitt, M. Venier, J. Leuker, and H. J. Andrä, submitted to *Phys. Rev. Lett.* (unpublished).
- [36] D. C. Parks, R. Bastasz, R. W. Schmieder, and M. Stöckli, *J. Va. Sci. Technol. B* **13**, 941 (1995).

FIGURES

FIG. 1. Target chamber geometry. (a) The HCI beam collides with the target surface at an incident angle Θ . Electrons are emitted at an observation angle Ψ with respect to the target surface towards the spectrometer entrance lens. In most experiments, we chose $\Theta + \Psi = 90^\circ$. For $\Psi \gg 0^\circ$, electron emission originating from all interaction phases can be detected. (b) At grazing observation $\Psi = 0^\circ$, the detection of electrons emitted from below the surface is suppressed due to their damping on the long path through the bulk towards the spectrometer lens. Only electrons emitted from the above-surface zone are not affected such that spectral regions stemming from transitions of incoming or reflected projectiles gain intensity with respect to regions ascribed to below-surface emission.

FIG. 2. Experimental spectra of Ar^{9+} projectiles impinging at a fixed incident angle of $\Theta = 45^\circ$ and various energies on a $n\text{-Si}(100)$ surface. All spectra in this paper are normalized on the portrayed peak region between 160eV and 240eV. The error at the peak maximum of the ($E_{\text{kin}} = 121$ eV)-spectrum is smaller than 0.3%. With increasing incident energy E_{kin} , the 224eV-peak begins to outgrow the 232eV-peak and the main peak moves from 211eV to 208eV.

FIG. 3. Ar^{9+} spectra at $E_{\text{kin}} = 121$ eV and varying incident angles Θ . The intensities of the two subpeaks on the shoulder above 211eV alter with v_\perp in the same way as in Fig. 2. For the two geometries at $\Psi = 0^\circ$, a second broad peak region evolves around 198eV which we associate with emission from partially ionized incoming or reflected particles.

FIG. 4. Ar^{9+} spectra at $E_{\text{kin}} = 9$ eV and Θ as parameter. The perpendicular velocity component v_\perp is minimal in all four measurements and Θ_{eff} thus stays roughly constant due to the image potential. Due to our normalization method, the high-energy shoulder above 211eV is untouched by changing the nominal incident angle Θ . At $\Psi = 0^\circ$, the broad region around 198eV pops up again.

FIG. 5. Series of Ar^{9+} spectra taken at fixed angles $\Theta = 90^\circ$ and $\Psi = 0^\circ$ with varying E_{kin} . For $E_{\text{kin}} = 9$ eV and 121eV, we can still distinguish two separate peaks around 198eV and 211eV. For higher E_{kin} , the 211eV-peak disappears and the broad structure washes out while extending to lower energies. The 232eV-peak can only be found for minimum v_\perp .

FIG. 6. This histogram displays the energetic positions of *LMM* Auger transitions originating from neutral “hollow” Ar^{9+} atoms comprising all possible $(2p^5 3s^x p^y d^z)$ -configurations with $n_M = x + y + z \leq 9$. Angular coupling shifts have been neglected. The neutralization for configurations possessing less than $q = 9$ electrons in the *M*-shell has been established via $(q - n_M)$ “spectator” electrons in the *N*-shell. Each transition has been weighted by unity discarding transition rates and statistical factors due to different subshell occupations.

FIG. 7. Potential V_{eff} (schematic) induced by an HCI core which is embedded into an electron gas. $V_{\text{Coul}}^{\text{free}}$ denotes a free ionic Coulomb potential. By adding outer spectator electrons to the atom, a screened Coulomb potential $V_{\text{Coul}}^{\text{screen}}$ forms which is implemented in our Cowan code calculations (spectator electron model). At large distances from the nucleus, the potential V_{eff} seen by an active electron merges into the bottom of the valence band V_0 . Electrons occupying states above V_0 cannot be bound by the ionic core. They are lost to the valence band continuum. As level binding energies E_b^{nl} approach V_0 , level shifts ΔE_b^{nl} increasingly deviate from the spectator electron model.

FIG. 8. Binding energy ranges of hollow atom Ar^{9+} 3ℓ subshells as a function of the total *M*-shell population. Within the spectator electron model, the $3d$ shell moves above the bottom of the valence band V_0 as soon as more than five electrons populate this level. For comparison, we added the $2p$ level binding energies of C^{5+} and Ne^{9+} as a function of the total *L*-population n_L and a DFT calculation [27] for the Ne^{9+} -Al system.

FIG. 9. Simulation of the experimental (cf. Fig. 2) Ar^{9+} and Ar^{9+} spectra at $\Theta = 45^\circ$ for $E_{\text{kin}} = 2$ keV (a) 121eV (b) and 10eV (c). For the ($E_{\text{kin}} = 10$ eV)-simulation, a statistically distributed M -shell population with $\langle n_M \rangle = 2$ at the bulk entrance (see text) is implemented. The intensity ratios between the LMM transition subgroups as a function of E_{kin} display the same systematics as the experiment. For the $E_{\text{kin}} = 2$ keV, we enforce a correction for elastic and inelastic bulk damping by convolving the original spectrum with an exponential function of decay length of 3 a.u..

FIG. 10. Experimental spectra of metastable Ar^{8+} projectiles impinging at a fixed incident angle of $\Theta = 45^\circ$ and varying E_{kin} on a n -Si(100) surface. Despite the initial $3s$ electron, the general shape of the spectra is very similar to the corresponding Ar^{9+} spectra in Fig. 2. Only the $3ss$ - and $3sp$ region intensities are slightly enhanced. The small peak at 247eV occurs at minimal v_\perp and can be assign to above-surface LMV_W emission [35].

FIG. 11. Experimental spectra of metastable Ar^{8+} projectiles impinging at $E_{\text{kin}} = 8$ eV and different incident angles Θ on a n -Si(100) surface. All spectra exhibit the small peak at 247eV as expected for the minimum perpendicular projectile velocity components v_\perp . At $\Psi = 0^\circ$, the broad peak around 198eV pops up again, cf. Figs. 3-5. In the $(\Theta = 5^\circ, \Psi = 0^\circ)$ -geometry, its intensity is reduced with respect to the 211eV-peak as compared to the corresponding Ar^{9+} spectrum in Fig. 3.

TABLES

| process | $\Gamma_{3\ell_1\ell_2}^{\text{filled}}$ | $E_{\text{kin}} = 9 \text{ eV } (\langle n_M \rangle = 2)$ | $E_{\text{kin}} = 121 \text{ eV}$ | $E_{\text{kin}} = 2 \text{ keV}$ |
|---------|--|--|-----------------------------------|----------------------------------|
| $3ss$ | 3.31×10^{12} | 0.8% (2.0 4.5 0.1) | 1.0% (2.0 4.3 0.1) | 2.0% (2.0 4.1 0.1) |
| $3sp$ | 5.29×10^{13} | 15.9% (1.6 5.1 0.0) | 17.1% (1.7 5.1 0.0) | 22.1% (2.0 5.0 0.0) |
| $3pp$ | 1.98×10^{14} | 72.5% (1.4 5.5 0.0) | 70.0% (1.5 5.5 0.0) | 66.8% (2.0 5.4 0.0) |
| $3sd$ | 6.20×10^{14} | 5.3% (1.2 0.5 1.4) | 7.2% (1.2 0.4 1.5) | 7.4% (2.0 0.3 1.4) |
| $3pd$ | 1.65×10^{15} | 4.6% (0.6 1.5 1.4) | 3.7% (0.8 1.4 1.4) | 1.4% (1.5 1.2 1.2) |
| $3dd$ | 4.13×10^{14} | 0.8% (0.4 0.4 2.4) | 1.0% (0.5 0.2 2.3) | 0.4% (1.2 0.1 2.2) |

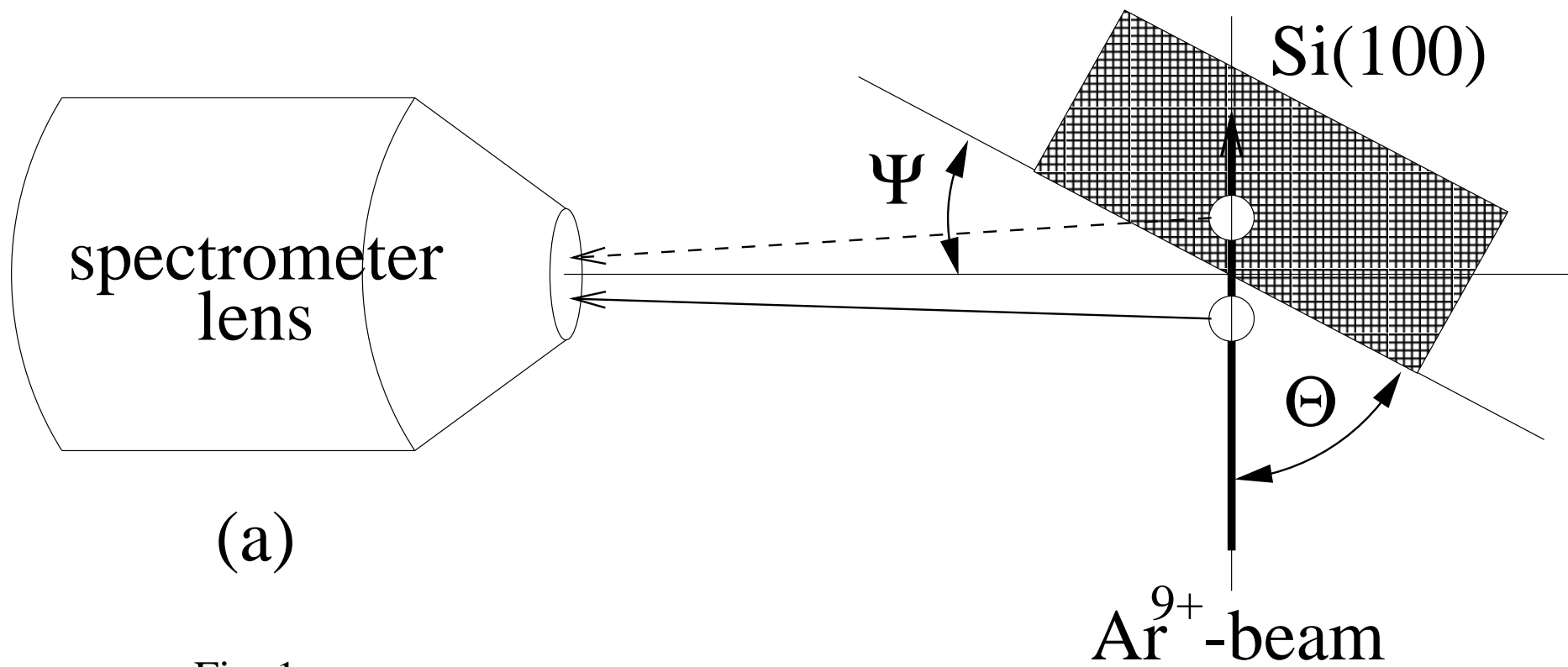
TABLE I. Monte Carlo simulation results on *LMM* processes for Ar^{9+} impinging on $\text{Si}(100)$ with $E_{\text{kin}} = 9 \text{ eV}$, 121 eV and 2 keV . $\Gamma_{3\ell_1\ell_2}^{\text{filled}}$ gives the *LMM* rate for a filled *M*-shell as required for the implemented fit formula [29]. For each simulation, we list the relative intensity and, in brackets, the average $(n_{3s}|n_{3p}|n_{3d})$ -configuration at the time of *LMM* decay which provides information about the evolution of the subsurface cascade.

| process | $E_{\text{kin}} = 9 \text{ eV } (\langle n_M \rangle = 2)$ | $E_{\text{kin}} = 121 \text{ eV}$ | $E_{\text{kin}} = 2 \text{ keV}$ |
|---------|--|-----------------------------------|----------------------------------|
| $3sdd$ | 66.2% (0.2 0.4 2.4) | 81.8% (0.2 0.2 2.4) | 11.7% (1.0 0.1 2.2) |
| $3pdd$ | 16.3% (1.0 0.2 2.8) | 21.0% (1.0 0.2 1.5) | 17.9% (1.5 0.1 2.4) |

TABLE II. Monte Carlo simulation results on *MMM* processes for Ar^{9+} impinging on $\text{Si}(100)$ with $E_{\text{kin}} = 9 \text{ eV}$, 121 eV and 2 keV . The table lists the average occurrence of each transition type and, in brackets, the average *M*-sublevel population at the time of *MMM* emission. Other sCK transitions are energetically forbidden.

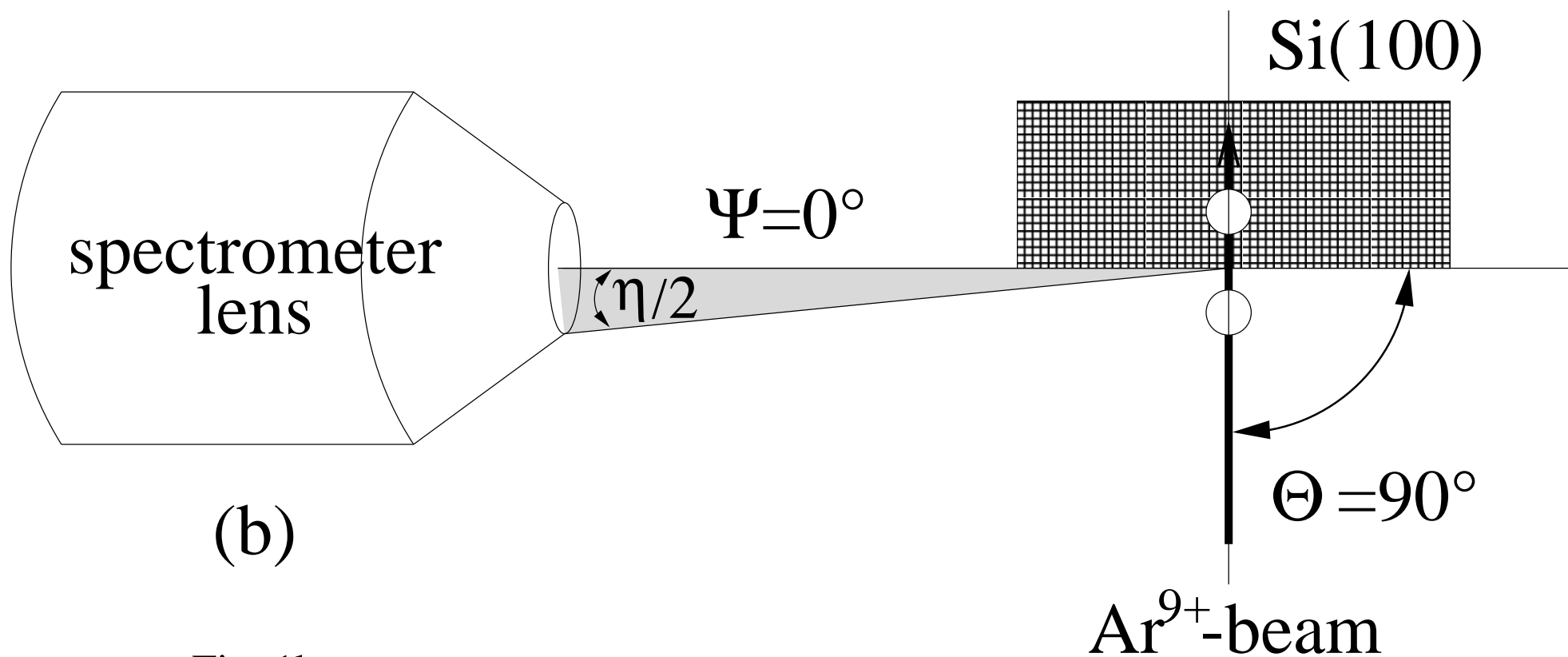
| n_M | $\Gamma_{3s}^{MCV} [\text{s}^{-1}]$ | $\Gamma_{3p}^{MCV} [\text{s}^{-1}]$ | $\Gamma_{3d}^{MCV} [\text{s}^{-1}]$ | $\Gamma_{tot}^{MCV} [\text{s}^{-1}]$ |
|-------|-------------------------------------|-------------------------------------|-------------------------------------|--------------------------------------|
| 0 | 9.92×10^{11} | 2.07×10^{12} | 6.61×10^{13} | 8.10×10^{14} |
| 1 | 1.21×10^{13} | 2.54×10^{13} | 9.18×10^{13} | 1.08×10^{15} |
| 2 | - | 3.26×10^{13} | 1.22×10^{14} | 1.41×10^{15} |
| 3 | - | 4.46×10^{13} | 1.44×10^{14} | 1.70×10^{15} |
| 4 | - | 6.53×10^{14} | - | 2.61×10^{15} |
| 5 | - | 5.78×10^{14} | - | 1.74×10^{15} |
| 6 | - | 4.48×10^{14} | - | 9.17×10^{14} |
| 7 | - | 3.27×10^{14} | - | 3.27×10^{14} |

TABLE III. *MCV* rates for the Ar^{9+}/Si system. The table lists *MCV* transition rates per spin state $\Gamma_{3\ell}^{MCV}$ for each *M*-sublevel and the overall *MCV* rate Γ_{tot}^{MCV} taking into account occupation statistics as evaluated by DFT calculations. n_M gives the initial number of *M*-electrons. The rates refer to initial *M*-shell ground state configurations. For $n_M = 0$, *MCV* processes filling the *3d* level possess by far the highest rates. As the subsurface cascade proceeds and $n_M > 4$, the *3d* level vanishes and the *MCVs* into the *3p* level rapidly populate the *M*-shell.



(a)

Fig. 1a



(b)

Fig. 1b

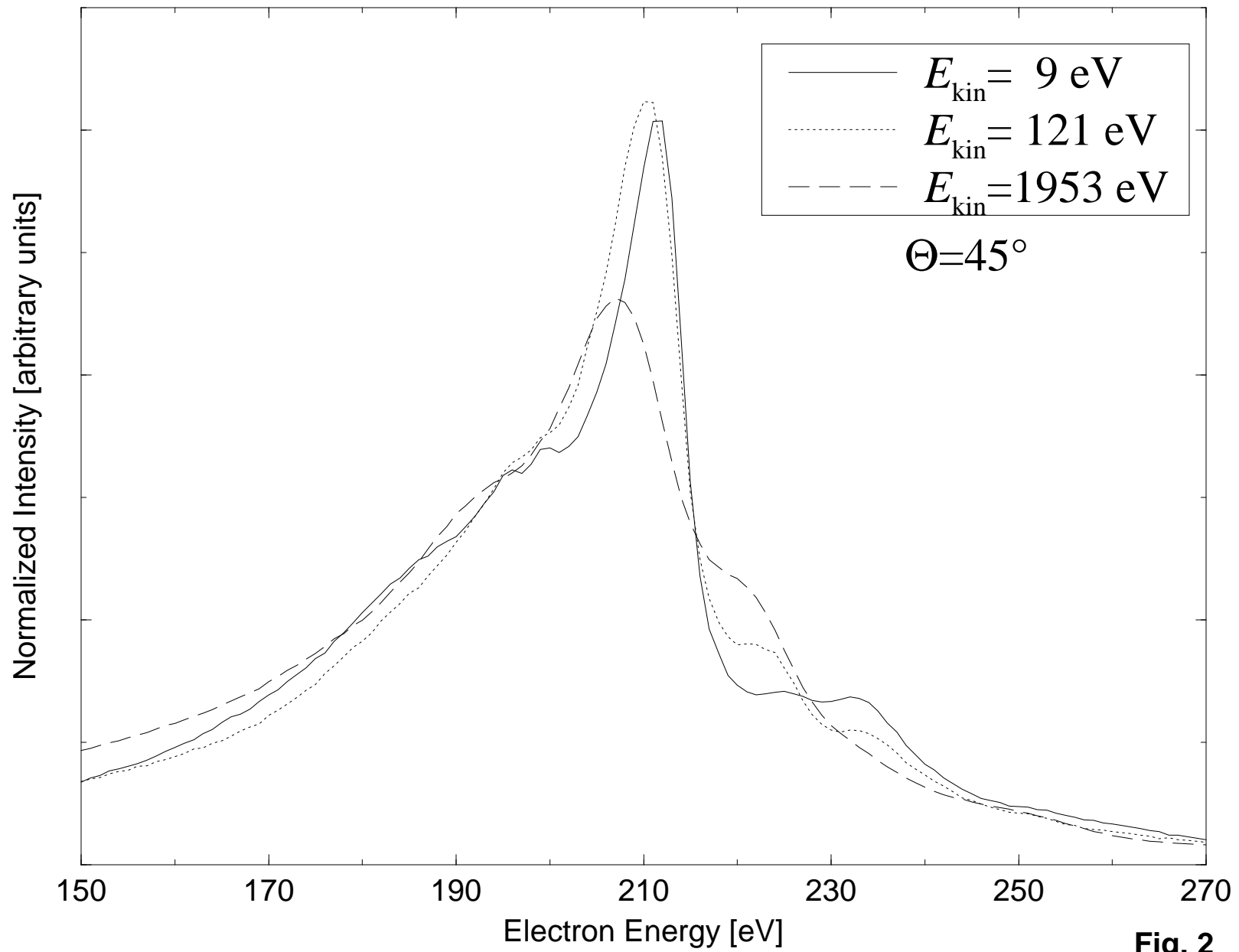


Fig. 2

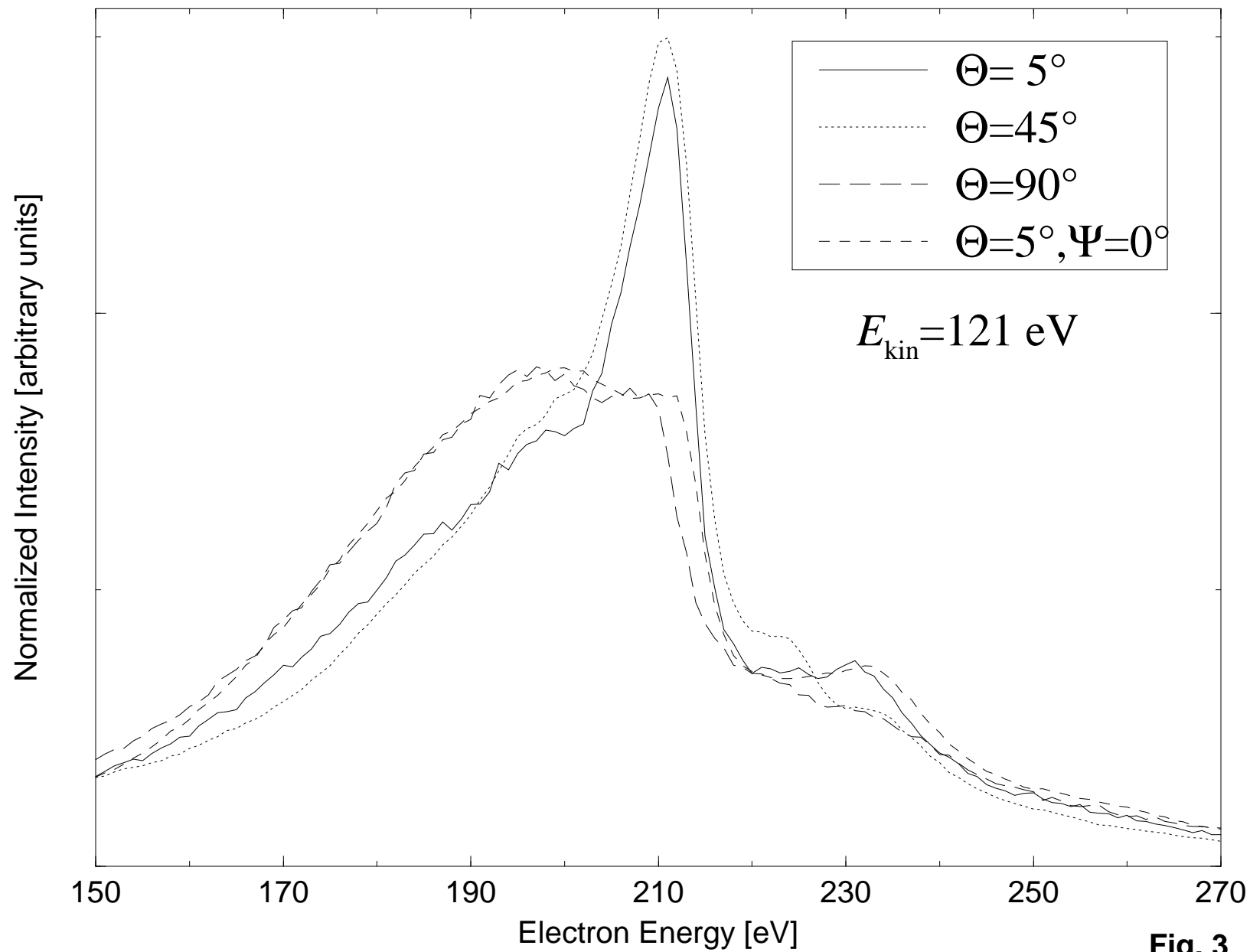


Fig. 3

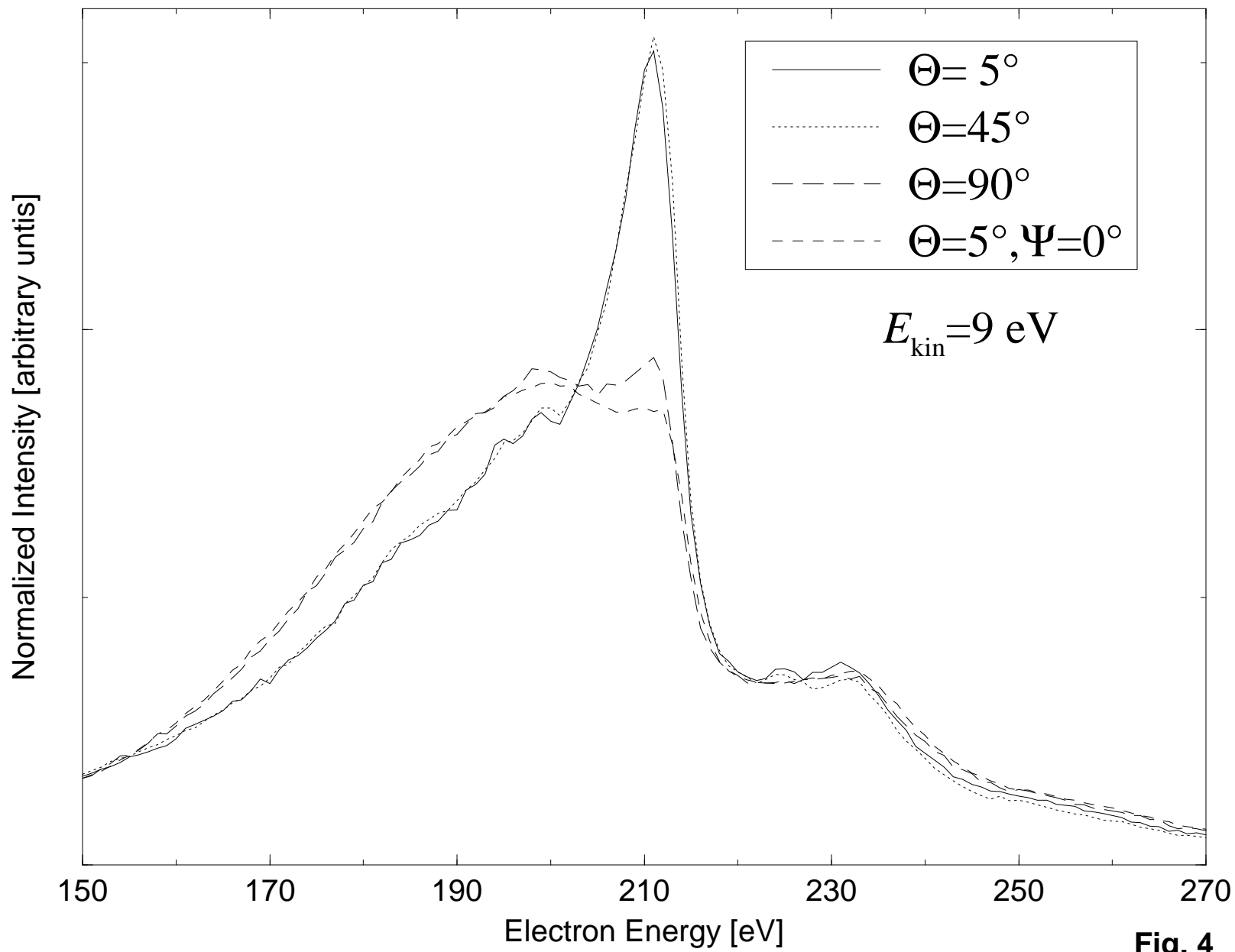


Fig. 4

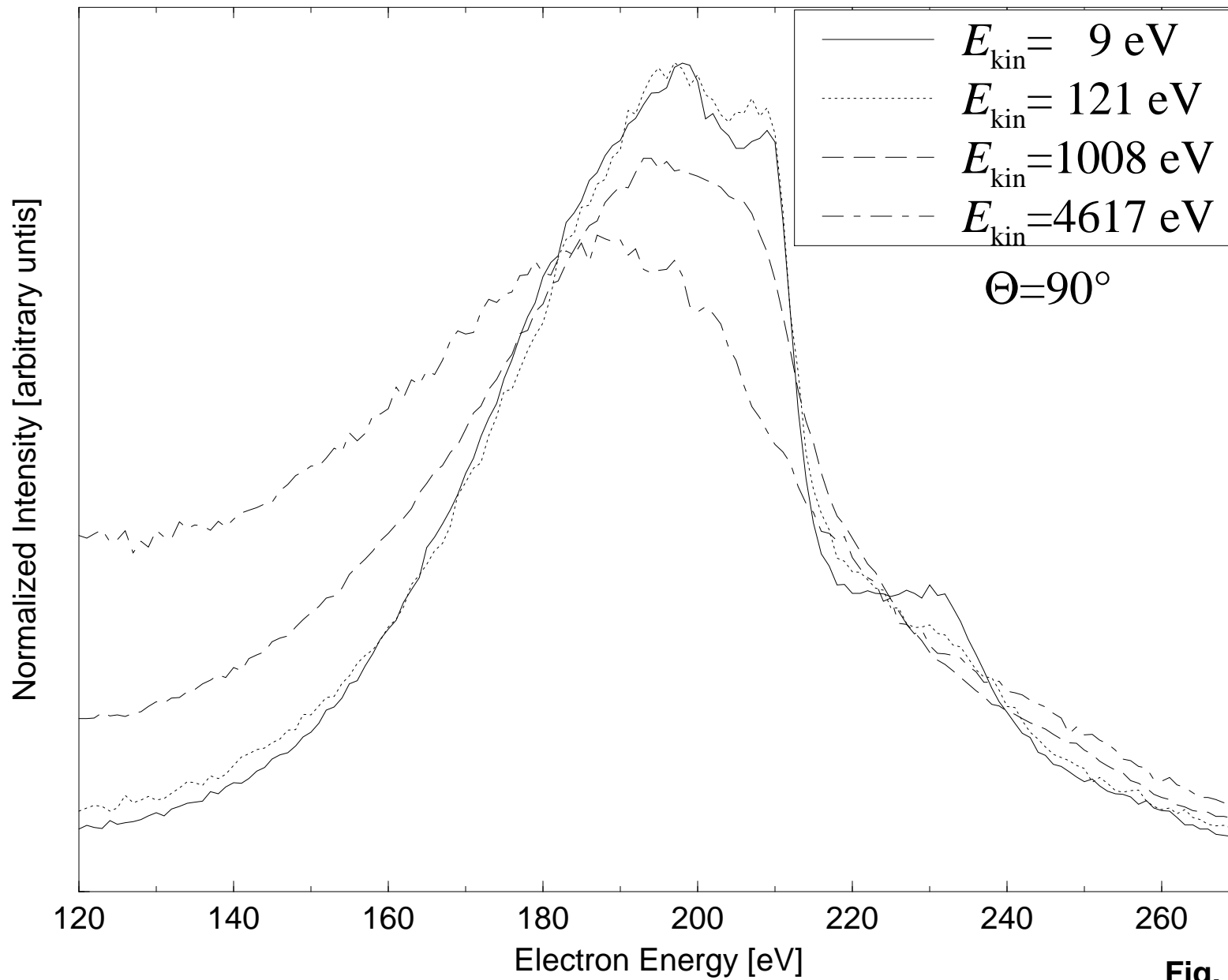


Fig. 5

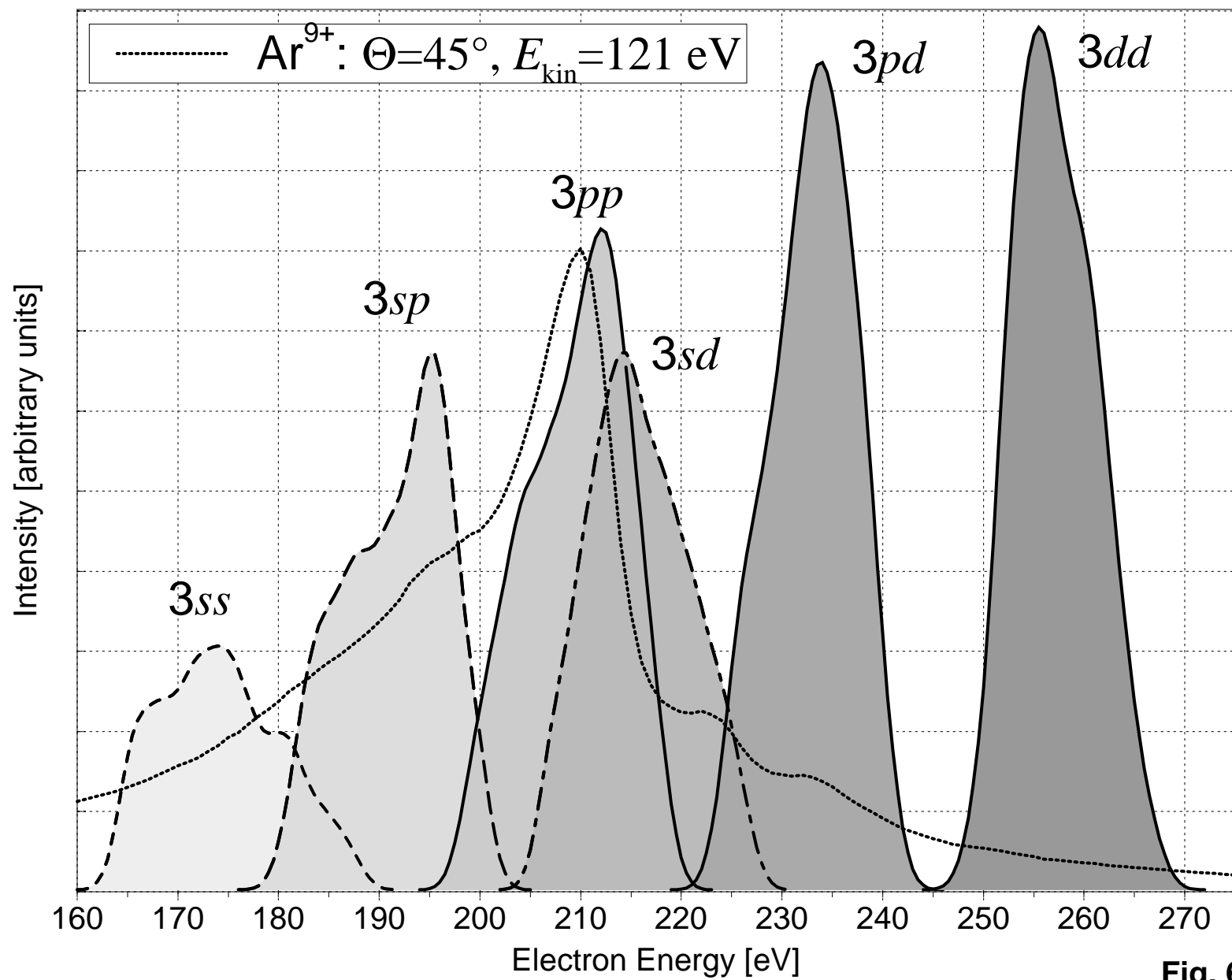


Fig. 6

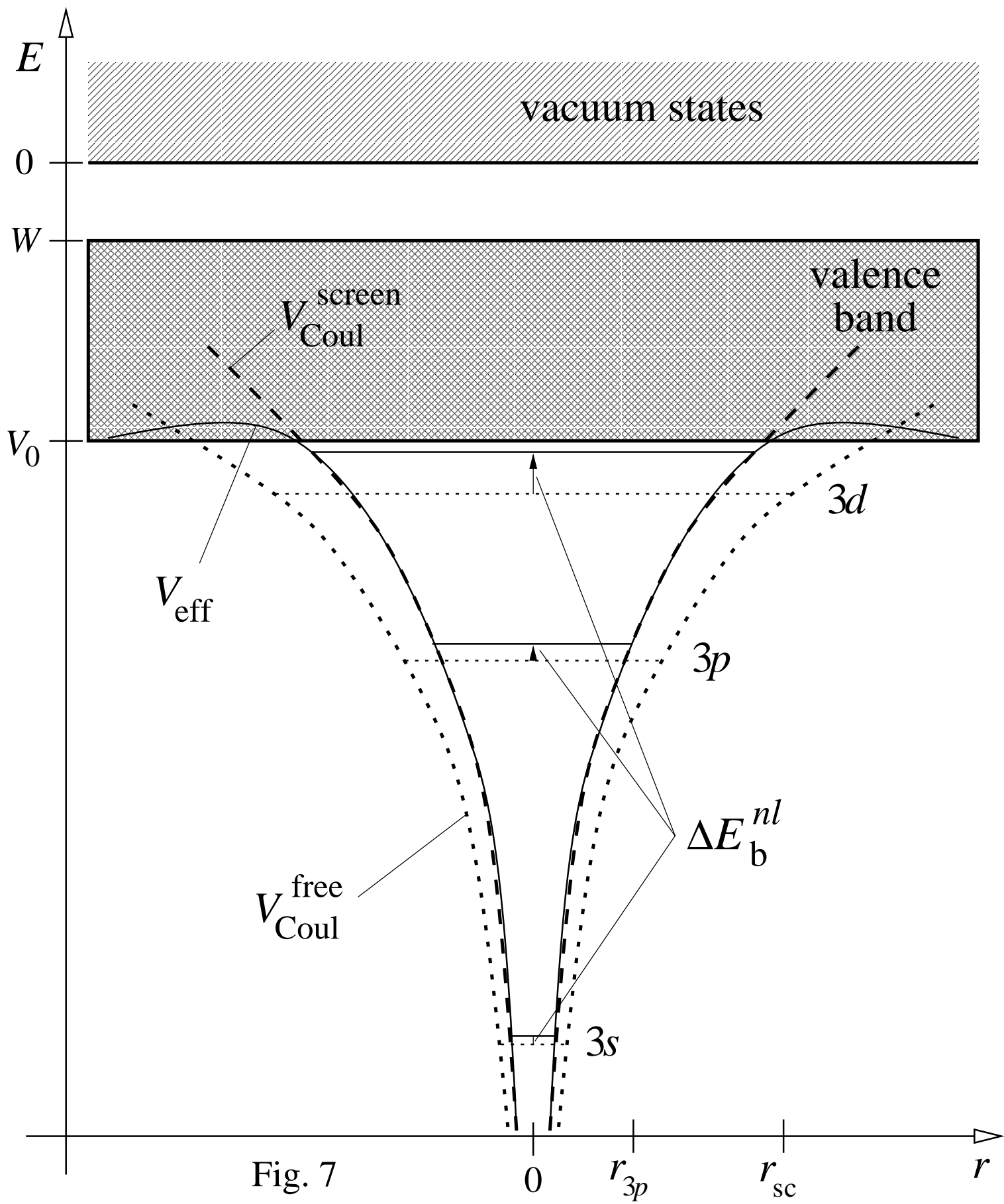


Fig. 7

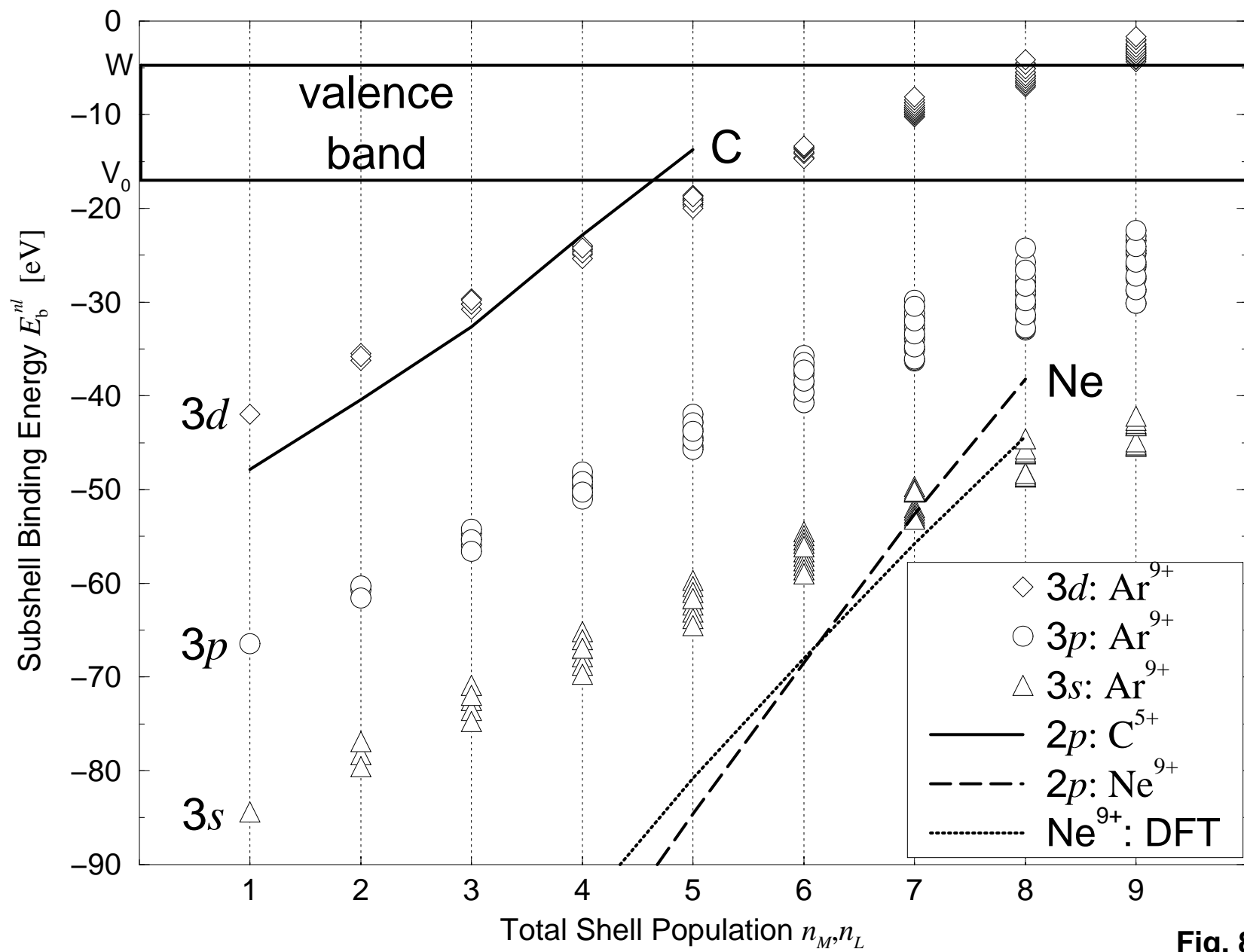


Fig. 8

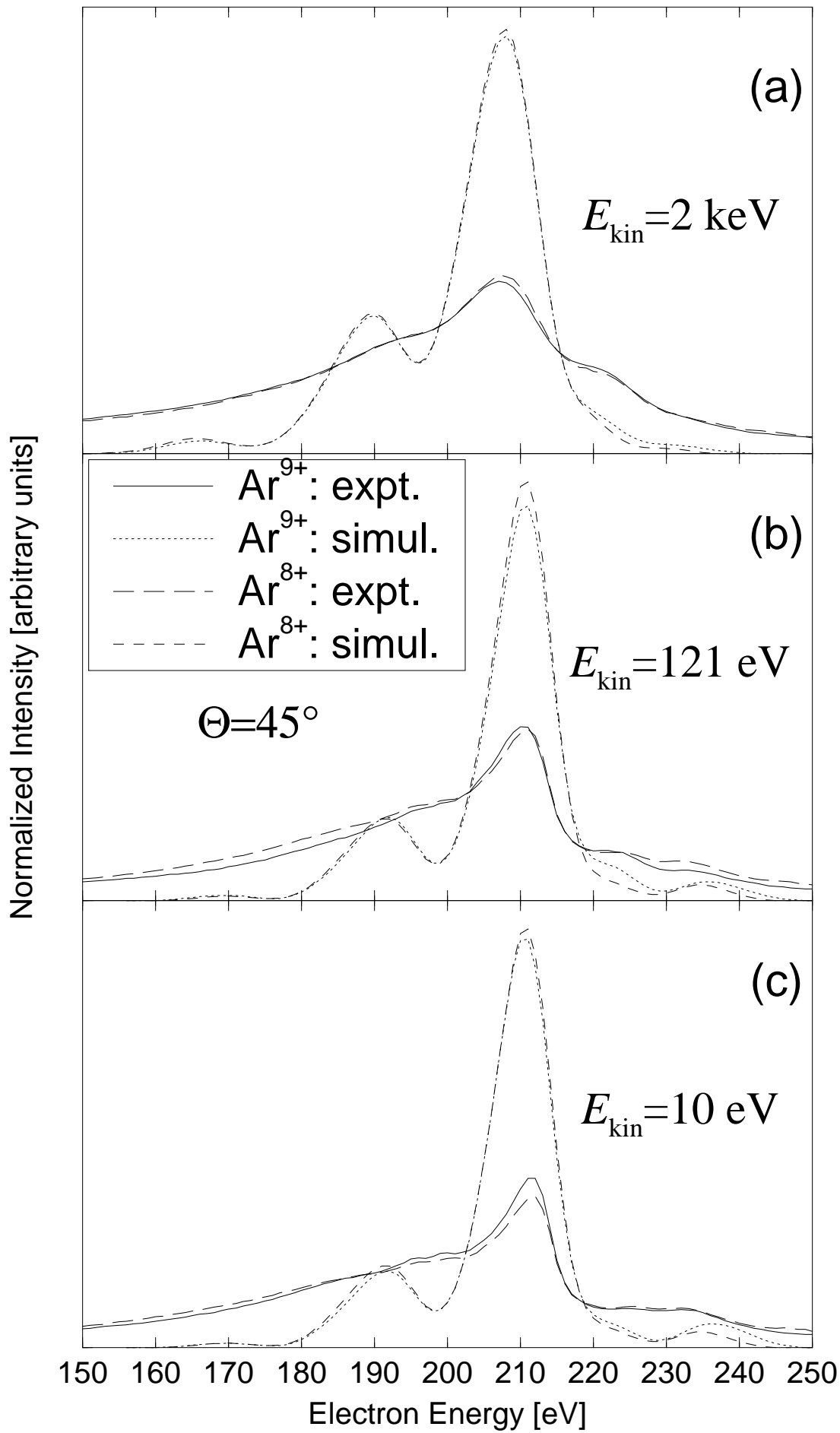


Fig. 9

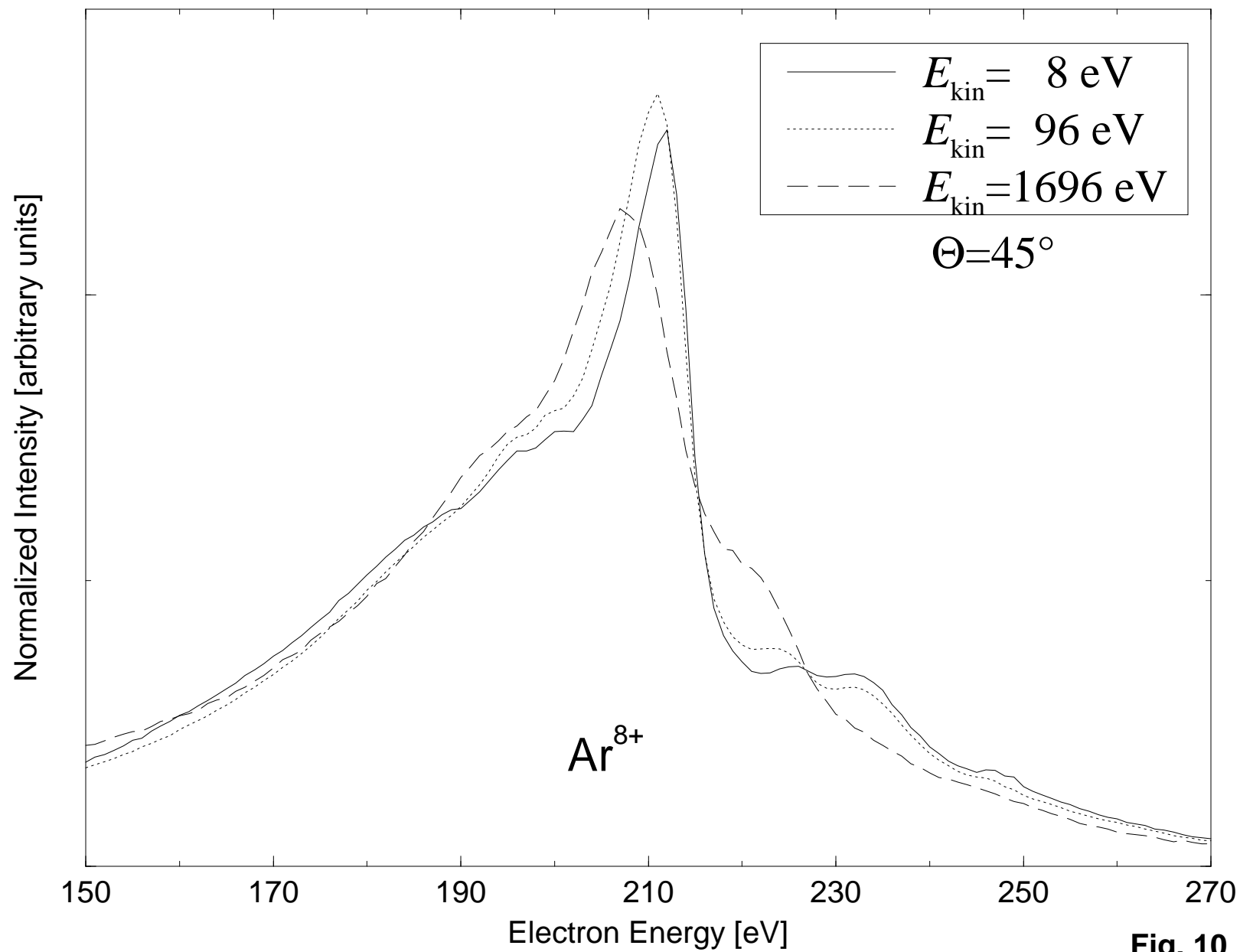


Fig. 10

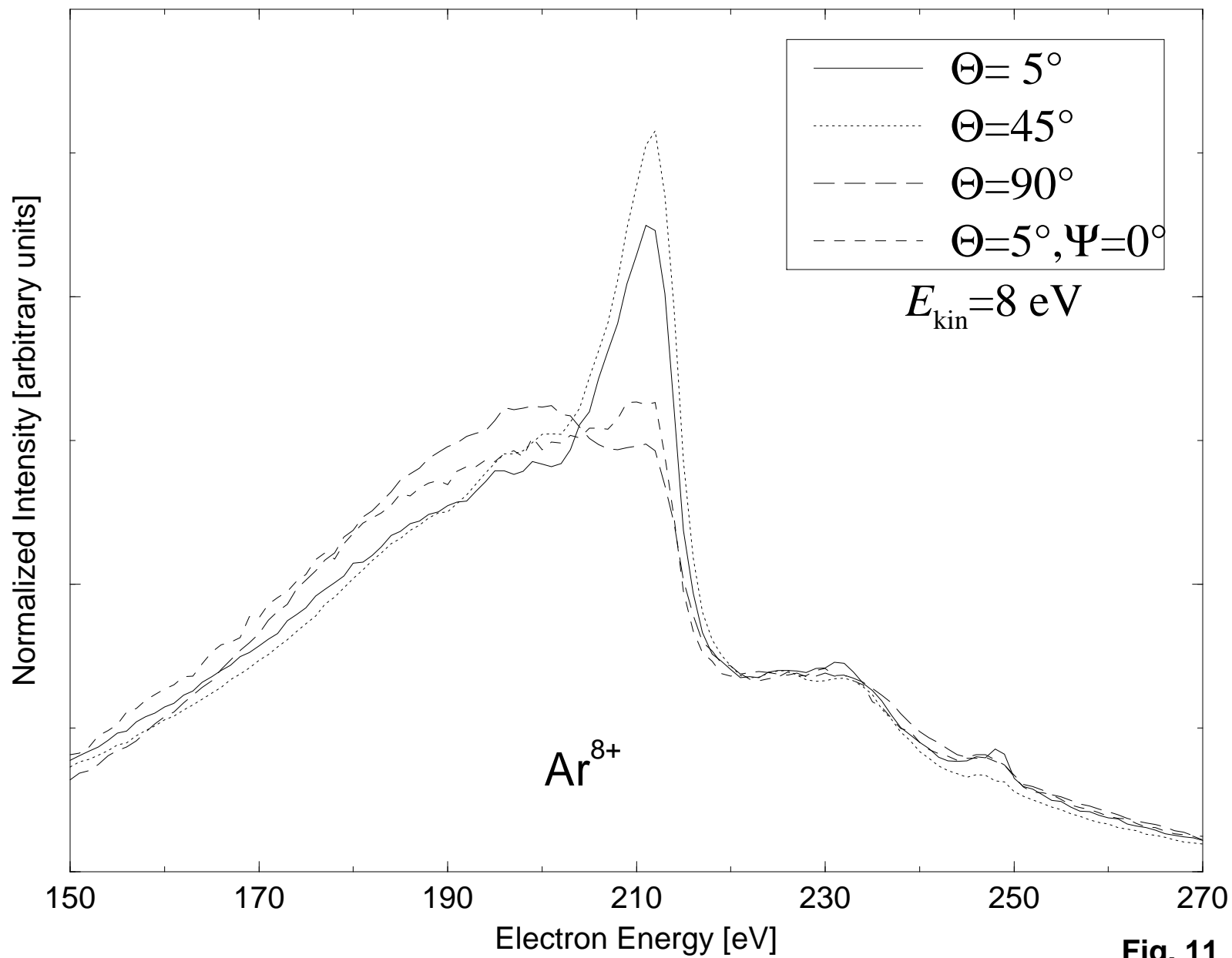


Fig. 11